

# An *HST*\* Morphological Survey of Faint EROs

David G. Gilbank<sup>1</sup>†, Ian Smail<sup>1</sup>, R. J. Ivison<sup>2</sup> and C. Packham<sup>3</sup>

<sup>1</sup>*Institute for Computational Cosmology, University of Durham, South Road, Durham, DH1 3LE*

<sup>2</sup>*Astronomy Technology Centre, Royal Observatory, Blackford Hill, Edinburgh, EH9 3HJ*

<sup>3</sup>*Department of Astronomy, University of Florida, 211 SSRB, Gainesville, Florida 32611, USA*

arXiv:astro-ph/0308318v1 19 Aug 2003

14 November 2018

## ABSTRACT

We present the results from a survey for Extremely Red Objects (EROs) in deep, high resolution optical images taken from the *Hubble Space Telescope* (*HST*) Medium Deep Survey. We have surveyed 35 deep F814W *HST*/WFPC2 fields in the near-infrared to a typical depth of  $K \gtrsim 20$ . From a total area of 206 arcmin<sup>2</sup> and to a limit of  $K = 20.0$  we identify 224 EROs ( $(1.14 \pm 0.08)$  arcmin<sup>-2</sup>) with  $(I_{814} - K) \geq 4.0$  and 83 ( $(0.41 \pm 0.05)$  arcmin<sup>-2</sup>) with  $(I_{814} - K) \geq 5.0$ . We find that the slope of the number counts of the  $(I_{814} - K) \geq 4.0$  EROs flattens beyond  $K \sim 19$ , in line with results from previous surveys, and the typical colours of the EROs become redder beyond the break magnitude. We morphologically classify our ERO sample using visual and quantitative schemes and find that 35% of our sample exhibit clear disk components, 15% are disturbed or irregular, a further 30% are either spheroidal or compact and the remaining 20% are unclassifiable. Using a quantitative measure of morphology, we find that the ERO morphological distribution evolves across the break in their counts, such that low concentration (disk-like) galaxies decline. We relate the morphological and colour information for our EROs and conclude that those EROs morphologically classified as bulges do indeed possess SEDs consistent with passive stellar populations; while EROs with dusty star-forming SEDs are mostly associated with disk-like and peculiar galaxies. However,  $\sim 30\%$  of disk EROs reside in the passive region of I/J/K colour-colour space. These could be either genuinely passive systems, lower redshift contaminants to the high-z ERO population, or systems with composite star-forming and passive SEDs. We use photometric redshifts for our high S/N multicolour photometry and derive redshift distributions in good agreement with spectroscopic work of somewhat brighter ERO examples.

**Key words:** cosmology: observations, galaxies: bulges, galaxies: peculiar, galaxies: starburst, galaxies: evolution, infrared: galaxies

## 1 INTRODUCTION

Broadband photometric selection is an increasingly common technique to identify high redshift galaxies (Steidel et al. 1999; Totani et al. 2001; Franx et al. 2003). One particularly powerful combination is to use optical and near-infrared passbands, typically  $R$  or  $I$  and  $K$ , to identify galaxies with a strong decline in their spectral energy distributions (SED) at wavelengths around  $1\mu\text{m}$ . These sources display extremely red optical-near-infrared colours, e.g.  $(I - K) \geq 4.0$ , and as such are termed Extremely Red Objects (EROs). This strong spectral decline could either result from a break in the SED or the suppression of bluer light due to strong dust

absorption. As we look at more distant galaxies, the first spectral break strong enough to produce such a red colour is the 4000Å break, which falls between the  $I$  and  $K$  passbands at  $z > 1$ . Progressively bluer features, such as the Balmer break (3625 Å) and Lyman-limit (912 Å), will fall in the relevant wavelength range for higher redshift sources, although these will typically be fainter than those systems selected on the basis of the 4000Å break. Similarly, the dusty systems within the ERO population are also expected to lie at high redshifts, due to the strong wavelength dependence of dust reddening combined with the redshifting of UV light into the optical passbands. ERO surveys thus enable us to identify both the most and least active galaxies at  $z \gtrsim 1$ , and hence provide a powerful probe of obscured star formation at  $z \gtrsim 1$  (Smail et al. 2002b, hereafter S02) as well as the nature of the evolved descendants of some of the earli-

\* Based on observations from the NASA/ESA *Hubble Space Telescope* obtained from the ESO/ST-ECF Science Archive Facility.

† Email: D.G.Gilbank@durham.ac.uk

est phases of star formation in the Universe (Dunlop et al. 1996; Zepf 1997).

Unfortunately, the mixed nature of the ERO population, compounded by the strong angular clustering of one or both sub-populations (Daddi et al. 2000), has led to a vigorous debate about the relative importance of the evolved and active components in the overall ERO population (Cimatti et al. 2002; S02).

The deepest ERO surveys undertaken show a rapidly increasing surface density of sources as a function of magnitude limit down to  $K \sim 19$ . Fainter than this, the increase in the numbers of EROs with apparent magnitude slows dramatically (Smith et al. 2002a; Firth et al. 2002). This transition is very abrupt and suggests that there may be a profound change in the nature of the EROs fainter than  $K \sim 19$ , perhaps associated with a variation in the relative proportion of passive and active systems at fainter magnitudes (Smith et al. 2002a; S02). To investigate this possibility we need an observational test to distinguish between the different sub-classes of EROs. There are three approaches which have been used to attempt to differentiate passive from dusty/active EROs: photometric tests, dust-insensitive star formation indicators and morphological classification.

The photometric classification of EROs was popularised by Pozzetti & Mannucci (2000), using  $J$ -band photometry to separate the two sub-classes on the  $(I - K) - (J - K)$  plane. Subsequent application of this test to various samples has led to the conclusion that the population at  $K \lesssim 20$  is roughly equally split between the dusty/active and passive sub-classes (Mannucci et al. 2002; Vanzella et al. 2002; Smith et al. 2002a; see also Cimatti et al. 2002). Unfortunately, without an independent test of this classification scheme it is hard to know how reliable these conclusions are.

Searches for millimetric and radio emission from samples of EROs have also been used to attempt to estimate the proportion of dust-obscured star-forming EROs in the overall population (Mohan et al. 2002; Wehner et al. 2002; S02). However, these star-formation indicators, while being insensitive to dust obscuration in the galaxies, are only capable of detecting the most vigorously star-forming systems at  $z \gtrsim 1$ . As a result they provide only a lower-limit of  $> 10\%$  (Mohan et al. 2002) and  $> 30\%$  (S02) on the proportion of star-forming systems in the ERO population. S02 also compare the colours of their radio-selected star-forming EROs with those expected for dusty star-forming and passive galaxies and find that most fall on or within the model classification boundary for dusty galaxies, providing some support for the Pozzetti & Mannucci (2000) scheme.

The final observable which has been used to differentiate between evolved and active ERO populations is their morphologies. It is commonly assumed that the passive EROs will have elliptical or at least early-type (Moriondo et al. 2000; Smith et al. 2002b) morphologies, while star-forming galaxies are expected to exhibit either a disk-like, disturbed or obviously interacting morphology (Dey et al. 1999). Morphological studies of very red galaxies have indeed shown that some have elliptical morphologies (Menanteau et al. 1999; Treu & Stiavelli 1999). However, results on statistical samples of EROs have produced more mixed conclusions, with Moriondo et al. (2000) and Roche et al. (2002) claiming a high early-type fraction and more recent work

by Smith et al. (2002a) and Yan & Thompson (2003, hereafter YT03) arguing for a more equal mix of early-type and later-type/disturbed systems. By comparing this classification scheme with those described above it is possible to test the reliability of the different approaches for a large sample of EROs (c.f. Smith et al. 2002a).

We highlight the study of YT03 which has very similar goals to those described in this paper. Their work utilised high resolution *HST* WFPC2 F814W-band imaging to morphologically classify a sample of 115 ( $I_{814} - K \geq 4.0$ ) EROs selected from ground-based  $K_s$ -band imaging to a  $5\sigma$  depth of  $K_s \lesssim 18.7$ . The authors visually classified their objects and found a mix of around 30:64:6 for bulge dominated, disk dominated and unclassified classes, with around 17% of the sample showing signs of merger/strong interaction. They showed their visual estimates to be in generally good agreement with an automated bulge+disk decomposition technique. The key improvement of our study over that of YT03 is that our near-infrared imaging is sufficiently deep to probe beyond the break in the ERO counts at  $K \sim 19$ . We also improve upon their work through the addition of multicolour photometry to test the different techniques for sub-classification of the ERO population.

We discuss our near-infrared observations of a selected sample of deep *Hubble Space Telescope* WFPC2 images in §2, present our analysis of these in §3 and the results which this provides are presented and discussed in §4, before giving our conclusions in §5. Throughout we assume a cosmology with  $\Omega_m = 0.3$ ,  $\Omega_\Lambda = 0.7$  and  $H_0 = 70 \text{ km s}^{-1} \text{ Mpc}^{-1}$ .

## 2 OBSERVATIONS AND DATA REDUCTION

A common misconception is that the key to a successful ERO survey is to obtain deep NIR imaging – in fact, the observationally most demanding aspect is achieving the necessary depth in the optical to identify that a galaxy is an ERO. For this reason, we have chosen to concentrate our survey on fields for which deep, high-quality optical imaging already exists. These fields come from the Medium Deep Survey (Griffiths et al. 1994) which consists of over 500 deep *HST*/WFPC2 images of intermediate/high-Galactic latitude blank fields. We selected a subsample of  $\sim 100$  fields from the parallel and pointed samples from the survey. These were selected by requiring only that the total exposure time in the F814W filter be greater than 4.0ks, that the primary target of any parallel observations was not a galaxy cluster or that, if the observations were pointed, that they were not targeting an extragalactic source (to ensure representative extragalactic regions) and that they be suitably placed for northern hemisphere follow up (Dec.  $> -10^\circ$ ). These then represent high-resolution (0.1 arcsec FWHM) and very deep ( $I_{lim} \sim 25\text{--}26$ ) images of random areas of the extragalactic sky.

### 2.1 Near infrared observations

Near infrared imaging was obtained using the Isaac Newton Group Red Imaging Device (INGRID, Packham et al. 2003)

on the 4.2m William Herschel Telescope (WHT)<sup>1</sup>. INGRID is a 1024<sup>2</sup> HAWAII-2 array at the bent Cassegrain focus of the WHT giving a 0.238 arcsec pixel<sup>-1</sup> scale and a 4.1×4.1 arcmin field.

Observations were made over 12 nights, 2000 November 13–15, 2000 December 9–11 and 2001 May 1–6. One night was lost due to the instrument being unavailable. A total of 55 fields were observed in the  $K_s$ -band and 30 of these in the  $J$ -band. Four of the nights were non-photometric, and we are in the process of obtaining calibration data for these. For the rest of this paper, we consider the bulk of the  $K_s$ -band data, 35 fields covering 206 arcmin<sup>2</sup> (*HST* +  $K$ -band coincident imaging) which are well calibrated. A summary of these fields is given in Table 1.

Each MDS field was imaged using a 9 point dither pattern with exposures of around 60s in  $K_s$  and  $J$  exposures of around 120s. Each  $K_s$  image was made up of 4×15s exposures coadded in hardware. The 9 point dither pattern itself was moved around the target field, in order to avoid bright objects falling on the same pixels. Total integration times are typically 2.8ks and are listed in Table 1.

The INGRID data were reduced using a custom written pipeline, available from <http://star-www.dur.ac.uk/~dgg/pipe/>. The pipeline uses standard IRAF<sup>2</sup> and STARLINK routines, and the reduction procedure is as follows.

### 2.1.1 Initial processing

The first step in the processing was to construct a bad pixel mask and apply a correction for an offset in the exposure time present in early versions of the software controller<sup>3</sup>. Dark subtraction was found to be unnecessary for most frames, but a master dark frame was subtracted if residual structure was seen. The data were flatfielded and sky subtracted using the *in-field chopping*, or *moving flatfield* technique of Cowie et al. (1990), using a running median of 8 temporally adjacent frames.

### 2.1.2 Mosaicking

Image registration and mosaicking was performed entirely using the STARLINK software CCDPACK. The first image of each target was taken as the reference and the relative offsets of the others calculated. This was achieved using the tasks FINDOBJ, FINDOFF and REGISTER to find objects in common between frames and calculate the offsets to sub-pixel accuracy. The images were then geometrically transformed with subpixel shifts and bilinear interpolation to conserve flux using TRANND, and finally combined using a 3- $\sigma$  clipped mean within the MAKEMOS task.

<sup>1</sup> Based on observations made with the William Herschel Telescope operated on the island of La Palma by the Isaac Newton Group in the Spanish Observatorio del Roque de los Muchachos of the Instituto de Astrofísica Canarias.

<sup>2</sup> IRAF is distributed by the National Optical Astronomy Observatory which is operated by AURA Inc. under contract with the NSF.

<sup>3</sup> [http://www.ing.iac.es/Astronomy/instruments/ingrid/ingrid\\_timing.html](http://www.ing.iac.es/Astronomy/instruments/ingrid/ingrid_timing.html)

The mosaic so produced is regarded as a first pass mosaic. In order to improve sky subtraction, a mask is made for all the astronomical objects in this image. SExtractor v2.2.2 (Bertin & Arnouts 1996) was used to detect and mask objects by making a CHECKIMAGE with the OBJECTS option.

The sky subtraction step is then repeated by first applying the de-registered mask to the images going into the local flatfield. In this way, objects too faint to be found in the individual exposures which would otherwise bias the estimate of the sky level and lead to oversubtraction of the sky can be successfully rejected (M. Currie, priv. comm.). The mosaicking step is then repeated with these second pass sky subtracted images to make the final mosaic.

In addition to the image mosaic, an exposure map is constructed by summing the number of images going into each pixel. This is used to deal with the uneven noise properties of the mosaics. An image with uniform pixel to pixel noise is generated by multiplying the mosaic by the square root of the exposure map. However, for the current dataset, the field of view of INGRID is very well matched to the WFPC2, allowing the latter to be entirely contained within the area of the former for any roll angle. Thus, no region of the WFPC2 field sees less than 100% of the near-infrared (NIR) exposure time, except the three pairs of fields suffixed 'XA' and 'XB'. These are fields where two overlapping MDS pointings exist, and the INGRID pointing lies midway between. Only NIR data with more than 50% of the total exposure time is considered in these three fields.

### 2.1.3 Non-photometric data correction

In the discussion of the mosaicking process above, no correction has been made to the photometric zeropoints for each individual frame going into the mosaic. This is because the extinction in the NIR is low ( $\lesssim 0.08$  magnitudes/airmass) and the fields were typically observed for around 2.8ks at low airmass, therefore the change due to the extinction variation from image to image is negligible. This is not the case for non-photometric data. However, it is straightforward to correct all the exposures of one field to the same zeropoint, as the interval between exposures is short, and the dither pattern is small, so there are many objects in common between frames.

To correct for non-photometric data, the first frame of a field was again taken as the reference image. The first pass mosaic was made as before, but when SExtractor was run on it to make the object mask, a catalogue of the 20 brightest objects in the field was output. After the second pass sky subtraction, aperture photometry was performed on these 20 objects and the optimal photometric zeropoint shift between each exposure and the reference calculated using the LINFIT task in IRAF. Typical shifts were  $\sim 0.1$  mag. The validity of this approach is verified through comparison with repeat observations made in photometric conditions, and with external photometry, described next.

### 2.1.4 Photometric and astrometric calibration

Calibration on to the UKIRT  $K$ -band system was performed using UKIRT Faint Standard (FS) stars (Hawarden et al.

**Table 1.** Table of observations. <sup>a</sup> – Field names are derived from MDS catalogue names. Fields suffixed XA and XB represent two overlapping *HST* exposures, with one corresponding *K*-band exposure targeted at the midpoint of the two; <sup>b</sup> – Target name is target of *HST* observation for pointed fields; PAR indicates a pure parallel field.

Field <sup>a</sup> ID	R.A. (J2000)	Dec	F814W T <sub>exp</sub> (ks)	F814W 5- $\sigma$ limit	K T <sub>exp</sub> (ks)	K 5- $\sigma$ limit	K seeing (arcsec)	Target <sup>b</sup>
UFG00	00 18 29.8	+16 20 39.4	4.7	25.06	2.8	20.09	0.73	PAR
UHG00	00 20 14.5	+28 35 22.6	5.6	25.75	2.6	20.29	0.94	PAR
UEH02	00 53 33.7	+12 50 24.1	4.2	25.58	2.8	20.11	0.95	PAR
UJH01	01 09 05.5	+35 35 35.9	4.2	25.27	2.8	20.11	0.73	PAR
UBI04	01 10 03.3	-02 25 19.8	5.5	25.64	2.8	20.25	1.10	PAR
UFJ00	02 07 03.3	+15 26 00.3	4.2	25.51	2.1	20.14	0.86	PAR
UGK00	02 38 49.5	+16 45 25.1	5.4	25.36	2.8	20.34	0.94	PAR
U2IY2	03 02 37.2	+00 12 32.4	6.4	25.49	2.8	20.21	0.76	FIELD-030233+00125
U2V12	03 02 42.6	+00 06 27.9	6.7	25.85	2.8	20.31	0.91	FIELD-030239+00065
U2IY1	03 02 46.2	+00 13 04.1	6.4	25.64	2.8	20.15	0.86	FIELD-030243+00132
U2V19	03 38 35.4	-00 12 38.3	6.7	25.77	2.8	20.28	0.97	FIELD-034112-00035
U2V17	03 40 58.1	+00 03 57.4	6.5	25.87	2.8	20.19	1.04	FIELD-034101+00030
U2V18	03 41 12.2	+00 00 28.4	6.7	25.91	2.4	21.10	0.68	FIELD-034115+00002
UPJ00	06 52 46.3	+74 20 43.6	4.2	25.37	2.8	21.06	0.69	PAR
UQJ10	07 27 36.9	+69 04 56.3	4.1	25.29	2.8	20.09	0.69	PAR
UQK02	07 41 33.5	+65 05 28.7	6.6	26.05	2.1	20.43	0.83	PAR
UQL00	07 42 41.4	+49 43 21.3	4.2	25.20	2.8	20.23	0.73	PAR
UOP00	07 50 47.1	+14 39 48.9	4.2	25.38	2.8	20.46	1.03	PAR
USP00	08 54 15.6	+20 02 47.0	4.2	25.28	2.0	19.85	0.66	PAR
UPS00	09 09 58.5	-09 26 51.9	5.6	25.76	2.8	20.17	1.20	PAR
UVM01	09 39 34.7	+41 33 37.4	4.6	25.23	2.8	20.03	0.76	PAR
UWP00	10 02 24.8	+28 51 01.8	8.4	26.13	2.8	21.96	0.81	PAR
UUS00	10 04 52.9	+05 15 52.3	4.6	25.45	2.8	20.53	0.71	PAR
UST00	10 05 47.9	-07 40 39.9	23.1	26.24	2.8	20.08	1.13	PAR
U2RJ1XB	11 48 47.8	+10 55 50.3	5.3	25.19	1.9	20.17	0.74	PAR
U2RJ1XA	11 48 50.7	+10 56 36.6	6.9	25.66	1.9	20.17	0.74	PAR
U2H92	13 12 14.6	+42 45 30.6	15.6	26.67	1.6	20.68	0.87	SSA13
UY401	14 35 30.7	+25 17 30.8	8.0	26.29	2.8	21.34	0.75	PAR
U2AY2	15 58 49.7	+42 06 18.3	25.2	26.70	2.2	20.44	0.88	DEEP-SURVEY-FIELD
UMD0EXB	21 50 32.7	+28 49 51.8	8.4	25.95	2.8	20.74	0.63	PAR
UMD0EXA	21 50 33.9	+28 48 29.0	5.6	25.67	2.8	20.74	0.63	PAR
UMD07XB	21 51 04.1	+29 00 33.1	9.6	25.84	2.3	21.04	0.88	PAR
UMD07XA	21 51 09.8	+29 00 39.6	8.7	26.35	2.3	21.04	0.88	PAR
UMD0D	21 51 25.6	+28 43 49.2	5.6	25.43	2.8	20.44	0.80	PAR
U2H91	22 17 35.7	+00 14 07.7	28.8	26.37	2.4	20.22	0.83	SSA22
U2V16	22 17 37.8	+00 17 14.3	6.7	25.84	3.4	20.06	0.95	FIELD-221736+00182
U2V14	22 17 59.3	+00 17 15.5	6.7	25.59	2.8	20.07	0.78	FIELD-221755+00171
UED01	23 19 52.2	+08 05 31.6	5.6	25.48	2.8	20.20	0.92	PAR
Median values			6.4	25.64	2.8	20.25	0.83	

2001). Several such stars were observed at the start and end of each night. The accuracy of the calibration was checked against the 2MASS All-Sky Point Source Catalogue<sup>4</sup>. Around 60% (including non-photometric nights) of the fields possessed sufficient bright objects in common with 2MASS to obtain an accurate test of the calibration. The minimum number of objects used was five, and more typically 10 - 20. Where the data overlapped, the agreement was found to be typically better than 0.05 mags. This also showed that zero point on non-photometric nights did not

differ from the nominal zero point estimated from the standard stars by more than  $\sim 0.3$  mags. We stress that we do not use data where the absolute calibration is more uncertain than  $\sim 0.1$  mags. All passbands are corrected for Galactic reddening using the maps of Schlegel et al. (1998). Astrometry was performed against the USNO-A2.0 astrometric catalogue (Monet 1998) using the package WCSTOOLS (Mink 1997) to automatically calculate the World Coordinate System (WCS) of the image, and found to be accurate to better than 1 arcsec.

<sup>4</sup> This publication makes use of data products from the Two Micron All Sky Survey, which is a joint project of the University of Massachusetts and the Infrared Processing and Analysis Center/California Institute of Technology, funded by the National Aeronautics and Space Administration and the National Science Foundation.

## 2.2 *HST* imaging

The *HST* images were retrieved from the ST-ECF Association archive. The archive takes all available associated data defined by the pointing of the telescope, performs an on-the-fly recalibration (OTFR) and co-adds these chip by chip.

The only additional processing necessary was to combine the four WFPC2 chips into a single mosaic. In so doing, the smaller pixel scale of the PC chip is resampled to that of the three WF chips. This was done using the IRAF STSDAS task WMOSAIC, which also corrects for the geometric distortion within the instrument. Photometric zeropoints were taken from the headers produced by the OTFR and are calibrated to the Vega system as described in Holtzman et al. (1995). The F814W Vega system is very close to the Cousins  $I$ -band and shall be referred to as  $I_{814}$  henceforth.

### 2.3 Image alignment and photometric catalogue

The seeing in the ground-based data was automatically determined by profile fitting to stellar objects in each frame. For each field, the *HST* data were then matched using Gaussian convolution to the seeing of the passband with the poorest seeing. All passbands were aligned to the  $K_s$ -band image and resampled to the INGRID pixel scale<sup>5</sup>, again using the STARLINK package CCDPACK to perform automated registration. The field of INGRID is astrometrically very flat, as is the WFPC2 field after geometric correction with WMOSAIC; thus the residual offsets between objects in the different passbands were typically at the level of one pixel. Although the internal astrometry of the WFPC2 device is very good, the external accuracy is somewhat lower, thus the WCS that we adopt in the catalogues is that of the  $K_s$ -band image.

Photometry is performed on coaligned images after convolution to the same PSF. These shall be referred to as the *convolved* images. Also, in order to exploit the exquisite resolution of the *HST*, we will wish to use the images prior to this transformation. We shall refer to these images as the *non-resampled* images. The CCDPACK software allows the mapping between our different coordinate systems to be readily stored, and provides a convenient way to transform between them.

SEXTRACTOR was used to detect objects brighter than the  $\mu_K = 21.2$  mag.  $\text{arcsec}^{-2}$  isophote, with at least 4 connected pixels ( $0.23 \text{ arcsec}^2$ ), after filtering with a Gaussian with a FWHM of 4 pixels ( $0.95 \text{ arcsec}$ ). This limit is determined from our shallowest fields, in order to ensure high uniformity in the object catalogues. Object detection was run on the uniform noise mosaic, described above. Photometry is performed by running SEXTRACTOR in double image mode, using the detection image to define the location of photometric apertures and measuring magnitudes from each convolved passband in turn (note that  $K$ -band magnitudes were measured from the  $K_s$ -band image, *not* from the  $K_s$ -band uniform noise image). An aperture diameter of 2.5 times the FWHM of the seeing was used. This ensures high signal to noise within the aperture (Lilly et al. 1991), and is small enough (typically around 2 arcsec) to avoid contamination from neighbouring objects, due to the good seeing of our data. We verified that our choice of photometric aperture is robust, by also examining colours defined by a fixed 2 arcsec aperture, a 4 arcsec aperture, and ‘total’ colours measured using the SEXTRACTOR BEST\_MAG in

<sup>5</sup> Hereafter, *pixel* shall refer to this common pixel scale of  $0.238 \text{ arcsec}$  unless explicitly stated otherwise.

each band (where the BEST\_MAG aperture is defined from the  $K_s$  image). It was found that all these measures are consistent, but that our adopted approach typically yields the colour with the smallest error.

Total magnitudes are measured for the  $K$ -band using the SEXTRACTOR BEST\_MAG.  $5\sigma$  limiting magnitudes within these apertures were calculated using SEXTRACTOR’s estimate of the signal to noise for each object detected (Table 4). The adopted  $5\sigma$  limiting aperture magnitude for the survey is  $K \leq 20.0$ , and only objects brighter than this are considered.

To assess completeness, a set of simulations was run first by inserting artificial point sources and then artificial elliptical and disk galaxies (of the typical size of faint galaxies in the survey) into our  $K_s$ -band images. Our detection procedure was then repeated on these. The typical completeness for point sources is greater than 80% at  $K = 20.0$ , and a similar completeness level is reached around 0.3 mag brighter for objects with de Vaucouleurs profiles. The simulations show we are 80% complete for compact sources at  $K=20.0$ ; while they also show that the sample is 100% complete for point sources around  $K=19.4$ , de Vaucouleurs profiles at  $K=19.1$  and the intermediate case of exponential disk profiles is 100% complete around  $K=19.2$ . Since our primary aim is to interpret the morphologies of EROs in the context of our survey and previous imaging surveys, which are typically selected to a limiting  $5\sigma$  depth, we apply this selection to our sample. A discussion of the completeness for different morphological types will be considered in future work, when comparing our data with galaxy formation models. In order to assess the spurious detection rate, the detection images were multiplied by  $-1$  and the detection and measurement procedure repeated. No false detections brighter than  $K = 20.0$  were found.

## 3 ANALYSIS

Our analysis will proceed by using our  $K$ -selected galaxy survey to isolate Extremely Red Objects based on their  $(I_{814} - K)$  colours. We will use the superlative resolution of the *HST* imaging to morphologically classify these EROs. Both qualitative visual classification and automated machine-based classification schemes will be used. We shall then compare our photometry, number counts and morphological fractions with previous work.

### 3.1 ERO sample selection

EROs were identified by selecting all objects matching the common definition (e.g. S02, Wehner et al. 2002, Roche et al. 2003, YT03) of an ERO of  $(I_{814} - K) \geq 4.0$ . Our goal is to determine the morphological mix of such EROs to  $K \sim 20$ . The astrophysical motivation behind this colour selection is described in detail in Pozzetti & Mannucci (2000) and references therein. Briefly, this colour cut corresponds to the expected colours for a  $z \sim 1$  passively-evolving, old stellar population, but is much redder than the expected colours of normal field galaxies; only high-redshift, heavily dust-reddened, massive starbursts can have similar colours. Therefore, this colour cut isolates the most and least actively star-forming galaxies at  $z \gtrsim 1$ .

Fig. 1 shows the colour-magnitude diagram for the whole  $K$ -selected survey. Our ERO catalogue was visually inspected and a small number of sources were rejected as being false detections, either being saturated stars or objects lying in the periphery of bright stars. No other false detections were found. We emphasize that for our entire survey, the NIR data used is highly uniform across the entire WFPC2 field of view and does not suffer from reduced signal to noise at the edges, as can be the case for surveys undertaken with smaller NIR imagers (e.g. YT03). We class objects with a SExtractor CLASS\\_STAR  $\leq 0.97$  as galaxies. Only one of our EROs would be classed as stellar by this definition (ERO082). We include this object for completeness (it may still be extragalactic, e.g. AGN, and will be morphologically classified from WFPC2 imaging later) but note that its inclusion has a negligible effect on our results.

We identify 224 sources to  $K \leq 20.0$  with  $(I - K) \geq 4.0$  and 83 with  $(I - K) \geq 5.0$  across the 206 arcmin $^2$  of our survey.

### 3.2 Morphological analysis

Using the exquisite resolution of the WFPC2 we can morphologically classify the EROs in our survey. This classification will proceed in two ways: we will use a scheme based on visual inspection of the images and also a quantitative system using machine-based measurements of the central concentration of each object. Each method has its own advantages and disadvantages: visual classification is somewhat subjective, but is better suited to deal with unusual objects, not well-fit by a model; whereas automated classification should be reproducible for a given set of input parameters, but unusual objects may lead to catastrophic misclassifications – e.g. for a merging system, the software might only fit one subcomponent, considering it to be an isolated system.

For the morphological analyses, the non-resampled F814W images were taken, and residual cosmic rays were rejected using the IRAF task CRAVERAGE. Next the images were rebinned  $2 \times 2$  to increase the per pixel surface brightness sensitivity. The reduction in angular resolution from this procedure does not adversely affect the morphological classifications, but aids in classifying the lowest surface brightness systems, which would otherwise be unclassifiable.

#### 3.2.1 Visual classification

All the EROs were visually classified by one of us (IRS) following the scheme in Table 2. This scheme was devised to isolate the broad classes of objects identified on a first-pass through the dataset.

This procedure used the same display software employed by the MORPHS group when classifying faint galaxies in distant clusters (Smail et al. 1997). The software displays two images at different stretches of a  $10'' \times 10''$  region around the ERO from the non-resampled WFPC2 images, after they are smoothed with a  $0.2''$  FWHM Gaussian to reduce the shot noise. This was used in conjunction with a hard-copy of each thumbnail image displaying the  $K_s$ -band image of the ERO contoured over the F814W image to allow isolated  $i814$ -band components within a single ERO to be easily identified (e.g. Fig. 11).

**Table 2.** Visual classification scheme for the EROs, based on the WFPC2 F814W imaging. Classes are motivated by the properties of the sample and we bin these to describe disk-like (2, 5, 6) and bulge-like (3 and 7) systems.

Class	Description	#	%
0	Blank or too faint to classify	43	19.20
1	Compact (small and peaked)	32	14.29
2	Compact, disk	36	16.07
3	Compact, symmetrical	26	11.61
4	LSB, disturbed	1	0.45
5	LSB	6	2.68
6	Obvious disk	42	18.75
7	Spheroidal	7	3.12
8	Merger	13	5.80
9	Amorphous	18	8.04

We give the proportions of different morphological classes in our full  $K \leq 20$  sample in Table 2. In a testament to the depth of the *HST* imaging, less than 20% of these very red and very faint galaxies were unclassifiable in the WFPC2 images. For the remaining sources, 40% are compact (although these can still exhibit weak morphological features), a further 20% are relatively well-resolved, disk galaxies and the final 20% comprise a mix of low surface brightness (LSB), mergers, amorphous or clearly spheroidal galaxies. As we have stressed, these morphological classes were motivated by the properties of the ERO sample and hence we will need to combine and convert them to translate them into astrophysically interesting classes.

#### 3.2.2 Automated classification

Given the modest S/N of typical EROs in our WFPC2 imaging, we have chosen in our quantitative morphological analysis to concentrate on two simple measures of the light distribution within the EROs. These are the concentration index,  $C$ , and mean surface brightness,  $\mu$  (Abraham et al. 1994, 1996a,b). Measurements of  $C$  for the ERO sample were made using a modified version of SExtractor to calculate  $C = F_{0.3}/F_{1.0}$  where  $F_x$  is the integrated flux within an elliptical aperture which contains a fraction  $x$  of the total isophotal area, and  $x=0.3$  is the standard definition (Abraham et al. 1994). The error on this measurement was estimated from simulations. Grids of artificial galaxy images were constructed using the IRAF ARTDATA package and inserted into random blank sky regions of the non-resampled F814W image, and the scatter in the measurement of  $C$  for the same input profiles recorded as a function of apparent brightness of the galaxy. The measured variation in  $C$  with apparent brightness of the galaxy (for a fixed light profile) in these simulations also allows us to investigate the evolution in the morphological mix of the EROs as a function of magnitude in a quantitative manner.

### 3.3 External comparisons

#### 3.3.1 $K$ -band galaxy counts

As a check of our  $K$ -band photometry, in Fig. 2 we compare our galaxy number counts (for all  $K$ -selected galaxies,

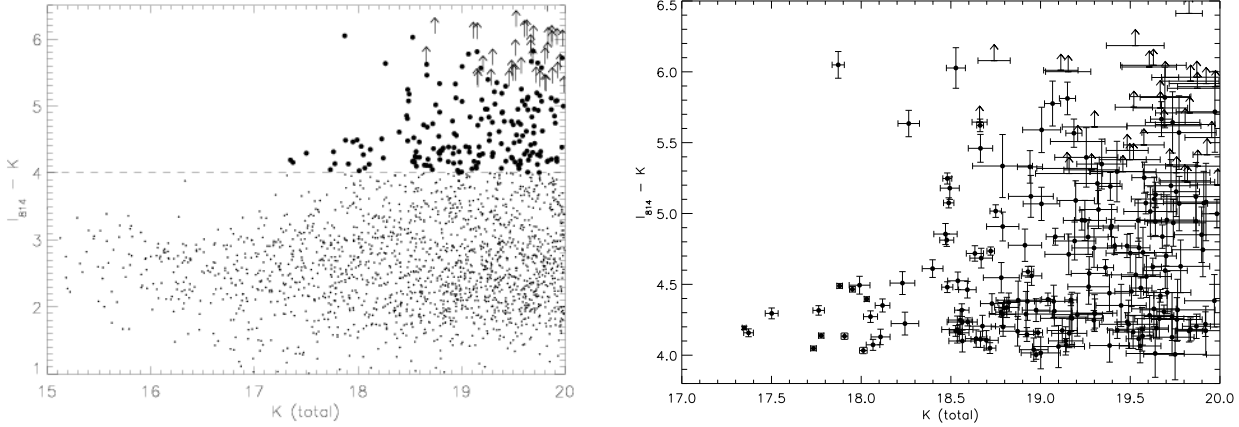


**Figure 1.** Colour-Magnitude diagrams for all galaxies in the survey (left panel) and for EROs (right panel) defined by  $(I_{814} - K) \geq 4.0$ . Error bars are omitted from the left plot for clarity and the broken line illustrates the  $(I_{814} - K) \geq 4.0$  ERO selection criterion. EROs are highlighted with bold points. Note the rapid increase in the proportion of the galaxy population in the ERO class at  $K > 18$  (4%), followed by a more constant distribution fainter than  $K \sim 19$  where the EROs contribute 12% of the total population.

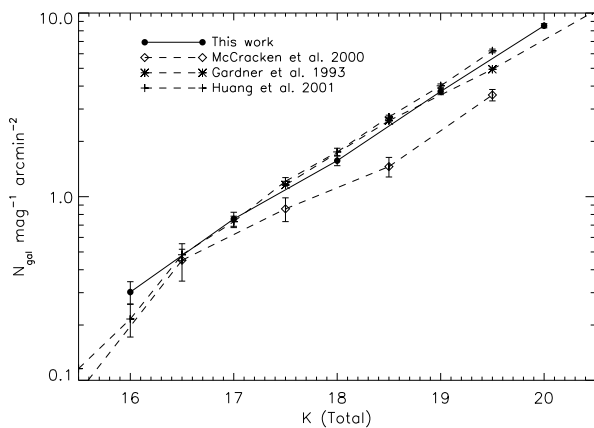


**Figure 2.** Differential  $K$ -band galaxy counts in half-magnitude intervals, corrected for incompleteness. Error bars simply assume Poisson statistics and are thus likely to be underestimates of the true errors. Selected number counts from the literature are also plotted. Our counts are in good agreement with other surveys.

irrespective of colour) with a selection from the literature. Our counts are in good agreement, showing a steep rise with gradient  $\alpha = 0.34 \pm 0.06$  to  $K \sim 20$ , with an incompleteness-corrected surface density of  $(7.5 \pm 0.2) \text{ arcmin}^{-2}$  at  $K=20$ .

### 3.3.2 ERO number counts

Firstly we consider the number counts of  $(I_{814} - K) \geq 4.0$  selected EROs in our survey. We compare our number counts to other datasets which use the same  $(I_{814} - K)$  selection to remove any concerns about differences in the samples due to the photometric selection (although see §4.7). This comparison is shown in the left panel of Fig. 3. Our cumulative ERO counts appear to show a break around  $K \sim 19$  and so we fit them using two power laws ( $\log_{10} N(K_1 < K < K_2) \propto \alpha K$ ), giving slopes of:  $\alpha = 0.88 \pm 0.09$  for  $K \leq 19.0$  and  $\alpha = 0.42 \pm 0.19$  for  $19.0 \leq K \leq 20.0$ . Also shown in

the figure are the counts of  $(I_{814} - K) \geq 4.0$  EROs from S02 (priv. comm.), Wehner et al. (2002), Roche et al. (2003) and YT03.

We see that our ERO counts are in excellent agreement with Roche et al. (2003), based on publicly available ESO imaging of the CDFS/GOODS. The S02 counts are marginally lower than the other data, but note that the error bars are purely Poissonian errors and likely to underestimate the true field-to-field variation (Daddi et al. 2000). At the faint end their number density agrees well with both ours and those of Roche et al. (2003). The counts of YT03 appear marginally higher but not significantly so.

We find an incompleteness-corrected surface density for  $(I_{814} - K) \geq 4.0$  objects of  $(1.14 \pm 0.08) \text{ arcmin}^{-2}$  to  $K \leq 20.0$ , representing 17% of the total galaxy population to this depth. This is in reasonable agreement with the value of  $(0.94 \pm 0.11) \text{ arcmin}^{-2}$  from S02 (using the same selection limits as ours, priv. comm.). Wehner et al. (2002) also find comparable numbers, but with large field to field scatter between their three fields, each of which uses a cluster lens to increase the sensitivity of their observations. The data shown in the plot excludes one of their three cluster fields (A2390) which seems particularly overdense in EROs. This further emphasizes the impact of field to field variations. The surface density to the magnitude limit of the YT03 survey also appears in good agreement with our estimate, and is consistent with the S02 point.

Next we consider a redder subsample selected by  $(I_{814} - K) \geq 5.0$ . We find a surface density of such objects of  $(0.41 \pm 0.05) \text{ arcmin}^{-2}$ , or 5% of the population to  $K = 20$ . The number counts of  $(I_{814} - K) \geq 5.0$  objects are adequately described by a single power law with a slope of  $\alpha = 0.70 \pm 0.02$ . Here we can only compare with the  $(I - K) \geq 5.0$  counts of S02 (priv. comm.) who find a surface density of  $(0.18 \pm 0.05) \text{ arcmin}^{-2}$ . Again we note that the error estimates do not include a contribution from clustering. We also note that this extreme colour cut is on the rapidly falling tail of the colour distribution (encompassing  $\sim 5\%$  of the population). Slight photometric offsets between different surveys leading to different colour measurements could

cause a large number of objects to be included or excluded. For example, if our two surveys measure colours systematically different by 0.2 mags (a reasonable calibration offset between ground based surveys), this is enough to allow our Poissonian error bars to overlap.

### 3.3.3 Comparison with YT03 photometry

We compare our photometric measurements with those of YT03. We have 15 MDS fields in common, from our sample of 35 and their sample of 77 MDS fields. Firstly we take the ERO catalogue of YT03 (their Table 2) and search for objects which lie in our survey fields (Table 1). We find 28 such objects (only 17 of which do we classify as EROs). Next we search our galaxy catalogues for entries within  $1''$  of the coordinates given by YT03. We match 26/28 objects. The remaining two (their u2v16#108 and u2v19#30) lie between the WFPC2 chips in our images and were thus masked from our analysis. The ST-ECF associations archive only includes data taken at very similar roll angles, so it is possible that YT03 included additional imaging not used in our analysis. Comparison of our F814W exposure times for the fields in question (U2V16 and U2V19) show identical exposure lengths to theirs. Therefore we believe that their inclusion of these objects in their catalogue is spurious.

We compare our  $K$ -band total magnitudes with their large-aperture ('total') magnitudes for these 26 galaxies and plot the results in Fig. 4. For 10/26 (38%) our estimates agree to within  $1\sigma$ , however, for 13/26 (50%) EROs YT03 measure considerably brighter  $K$ -band magnitudes, by 0.5–1 mag. This offset thus results in YT03 measuring redder ( $I_{814} - K$ ) colours for these galaxies and hence classifying them as EROs, whereas in our data they are bluer than  $(I_{814} - K) \geq 4.0$ . We visually examined the extreme outliers and can find no obvious reason for the discrepancy. For example, one such outlier with  $\Delta K = 1.21$  lies on the same WFPC2 chip as two other EROs which we measure to be the same brightness as YT03 to within 0.4 magnitudes. For these 26 galaxies, we measure a median offset of  $0.26 \pm 0.07$ . This slight photometric offset would bring their ERO number counts into closer agreement with ours and Roche et al. (2003). We emphasize that this comparison only uses data taken under photometric conditions and so cannot be affected by corrections for non-photometric images. We attribute the disagreement to the quality of the YT03 data, which is known to be shallower, more inhomogeneous and taken in poorer seeing conditions. For the case illustrated above, the seeing FWHM in their data is  $1.7''$ , compared with ours which is around  $1.0''$ . The poorer seeing means that a larger photometric aperture must be used, leading to a noisier measurement of the magnitude.

### 3.3.4 Comparison with YT03 visual morphologies

We directly compare our visual classifications with the classifications of YT03, for the 17 EROs in common between our samples. Though our classification schemes are different, we can bin both samples coarsely into disks, bulges and other. Our classes 2, 5 and 6 are disk dominated classes and broadly equivalent to their D, D+B and ID classes. We find 11 objects in common in these three classes. For spheroidal designations, we compare our classes 3 and 7 with their B and

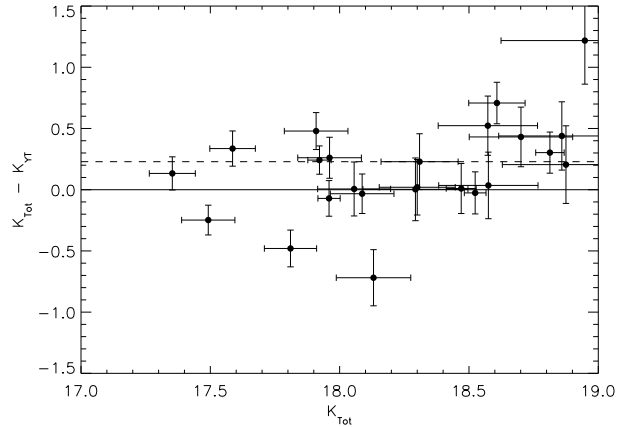


**Figure 4.** The comparison between our  $K$ -band photometry and that of YT03 for galaxies in common. We plot the difference between their large aperture magnitude and our total magnitude. Even though our total magnitude should encompass more light than their aperture magnitude, there is evidence that their  $K$ -band magnitudes are systematically brighter, by around 0.3 mag (indicated by broken line). See text for discussion.

BD. Here we find that one object we classify as spheroidal, YT03 class as a disk. Furthermore, two EROs which they class as bulges, we classify as disks. From our merger category (which has no equivalent in their work), we have two objects, one of which YT03 class as a bulge, the other as a disk; and we both agree that a final object is unidentifiable. Hence, through a very broad comparison with the YT03 classifications, we agree on 12 classifications, disagree on 3 and a further 2 (our merger category) we are unable to compare.

Next we examine the distributions of morphologies within our ERO samples. We restrict our catalogue to  $K \leq 18.7$ , the median  $5\sigma$  limiting magnitude of YT03, in order to compare the morphological mixes between the two surveys. From their visual classifications, YT03 found  $35 \pm 5\%$  of their EROs to be bulge-like and  $64 \pm 7\%$  to be disk-like with 6% unclassifiable (where the errors are simply Poissonian). Our visual classifications divided coarsely into bulge-like or disk-like classes (Table 3) yield  $24 \pm 6\%$  bulge-like and  $54 \pm 10\%$  disk-like with 8% unclassifiable. Note that here the 14% (7/50) of our classifications which do not fit into the simple bulge-like or disk-like (e.g. merger, amorphous) are not included. Hence, both our surveys find approximately twice as many disks as bulges at these magnitudes.

### 3.3.5 Comparison with MDS automated morphologies

A more detailed quantitative analysis of galaxy morphology in the MDS was performed by Ratnatunga et al. (1994, 1999). In outline, they applied a maximum likelihood fitting technique to the surface brightness profiles of MDS galaxies. The models they fitted were axisymmetric de Vaucouleurs and exponential disk profiles. A galaxy best fit by the former profile was classed as a bulge and the latter profile as a disk. If some combination of the two gave a better fit then the relative contribution of the two components was output in the form of a bulge to total luminosity ( $L_B/L_{Total}$ ).

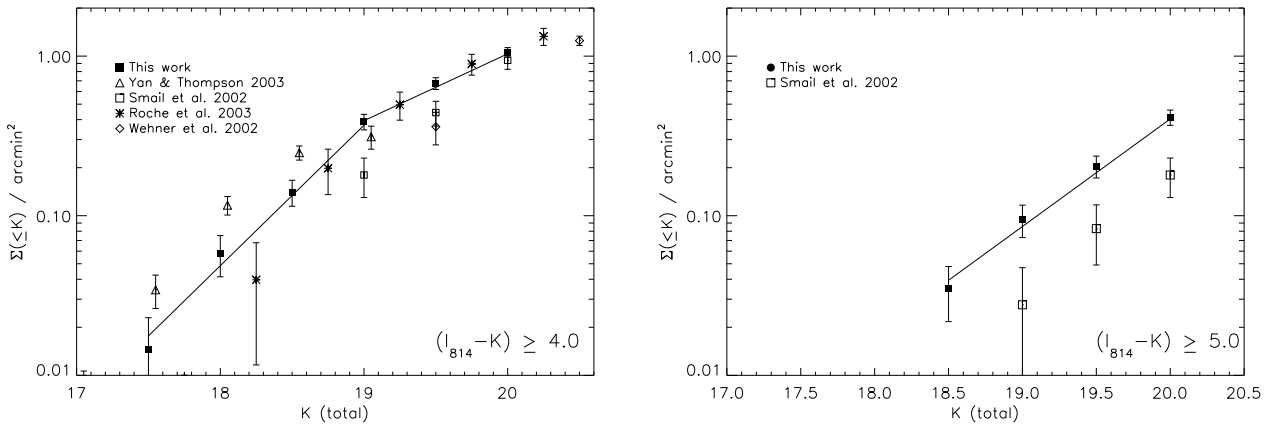


**Figure 3.** Surface density of EROs. Left panel shows cumulative number counts for the full ERO sample selected with  $(I_{814} - K) \geq 4.0$ . Overplotted are other ERO counts from the literature, with their selection criteria listed. Right panel shows the redder subsample selected with  $(I_{814} - K) \geq 5.0$  compared with the redder subsample of S02 (priv. comm.) using the same selection criterion. Solid lines are our power law fits.

The completeness limit for classification is drawn at  $\Xi = 1.8$  (where  $\Xi$  is their signal to noise index computed from the signal to noise of each pixel in an object) which corresponds to  $I \sim 24.5$  for the shallowest fields used here. A  $\Xi \geq 2.0$  (0.5 mags brighter) is required to class a galaxy as either disk-like or bulge-like (otherwise sources are just divided into either point or galaxy), and a  $\Xi \gtrsim 2.4$  is required to fit a bulge+disk model.

The reliability of this maximum likelihood estimate (MLE) was tested with the sophisticated and now widely-used two-dimensional surface brightness fitting algorithm of Simard (1998, GIM2D) by Simard et al. (2002). They found that the agreement of structural properties such as half-light radius and bulge to total light ratios between the classifiers was very good down to the limit studied of  $I_{814} \leq 22$ . A small fraction of objects were found to have very different bulge fractions as measured by the different classifiers, and most of these turned out to be peculiar or interacting systems. This emphasizes that automated classifiers are unable to deal robustly with unusual galaxies.

Morphological fractions for our ERO sample based on the MDS MLE results<sup>6</sup> are also tabulated in Table 3. 79 of our 224 EROs are unmatched with any entry in the MDS database. 10 have more than 1 match within 1''. We include these objects and take the nearest match. YT03 found that, for their sample, the MLE morphologies gave a mix of 50% disks and 37% bulges. Using the same scheme for our  $K \leq 18.7$  subsample, we find relative fractions of  $32 \pm 7\%$  disks and  $20 \pm 6\%$  bulges with 48% unclassified. 17 of this subsample of 50 are not listed in the MDS catalogue (Griffiths et al. 1994). Ignoring for the moment the objects without classifications, the MDS MLE classifications for the

<sup>6</sup> The Medium Deep Survey catalog is based on observations with the NASA/ESA Hubble Space Telescope, obtained at the Space Telescope Science Institute, which is operated by the Association of Universities for Research in Astronomy, Inc., under NASA contract NAS5-26555. The Medium-Deep Survey analysis was funded by the HST WFPC2 Team and STScI grants GO2684, GO6951, GO7536, and GO8384.

**Table 3.** Summary of the coarse morphological classifications for two of our ERO samples: the full sample and a subsample cut at  $K = 18.7$ , the median limiting magnitude of YT03. Two classification schemes are considered: our visual morphologies and automated maximum likelihood estimator (MLE) fits. <sup>†</sup> – Galaxies in our visual classification scheme which do not fit into either the disk or spheroid bins, and galaxies which are unclassified by the MDS MLE. See text for details.

Sample	Disks	Spheroids	Other <sup>†</sup>	Total
Visual				
$K \leq 18.7$	27/54%	12/24%	11/22%	50
Full	84/37%	33/15%	107/48%	224
MDS MLE				
$K \leq 18.7$	16/32%	10/20%	24/48%	50
Full	53/24%	33/15%	138/62%	224

YT03 sample find around 40% more disks than bulges; we find around 60% more disks than bulges. The general trends in these two surveys at bright ( $K \leq 18.7$ ) are consistent: visual classifications identify approximately twice as many disks as bulges and the MDS MLE method identifies approximately 60% more disks than bulges for those objects sufficiently bright to classify.

We have shown via direct comparison that our visual morphologies are in reasonably good agreement with those of YT03, with a disagreement at the level of  $\lesssim 20\%$ . The relative morphological mixes within both samples (YT03 versus our bright subsample) also appear consistent through both visual morphologies and automated bulge+disk decomposition. Thus we can now use our full sample to look at evolution across the break in the ERO number counts into the  $K = 19$ –20 regime.

### 3.3.6 Comparison with other morphological studies

Our morphological fractions contradict the findings of Moriondo et al. (2000) who found 15% irregular/disk-like,  $\sim 50$ –80% elliptical-like. Nevertheless, as they themselves

note, their sample is drawn from a heterogeneous collection of archival *HST* pointings and may not be representative. Roche et al. (2002) also find a high fraction of bulge-dominated EROs using ground-based *K*-band data ( $39 \pm 11\%$  bulge,  $25 \pm 9\%$  exponential disk profile systems) from a subsample of 32 of their EROs with high resolution UFTI data taken in good seeing. Unfortunately, ground based NIR data is not ideal for morphological studies, as even in the best seeing conditions, the very nature of the NIR observing strategy means that multiple, dithered images must be registered and combined, with the added complexity that the seeing may be changing between exposures. Correct propagation of all such uncertainties through the surface brightness profile fitting procedure is non-trivial. Furthermore, Roche et al. (2002) report a possible  $z \sim 1$  cluster of EROs comprising five bulge systems and two disks, thus inflating the early-type galaxy fraction.

Our morphological fractions are also in broad agreement with those from an *HST* imaging survey of lensed EROs given by Smith et al. (2002a) (18% compact, 50% irregular/disk-like and 32% unclassified) using an  $(R-K) \geq 5.3$  selection criterion. Although, we caution that  $(R-K) \geq 5.3$  selection may find different systems from  $(I-K) \geq 4.0$  selection (see §4.7).

## 4 RESULTS & DISCUSSION

### 4.1 Evolution of ERO colour distribution

To search for changes in the ERO population across the break in the number counts, we will take subsamples of the 100 brightest and 100 faintest EROs in the survey, to maintain equivalent uncertainties in both bins. This corresponds to  $K < 19.16$  and  $K > 19.38$  for the bright and faint samples respectively. This is a good choice as, although the position of the break is not precisely defined, it seems to occur around  $K \approx 19.0-19.5$ .

The cumulative colour distributions of the ERO sample divided into bright and faint *K*-band bins are examined in Fig. 5. The distributions clearly appear different such that the fainter sample is skewed toward redder colours (with a median colour of  $(I-K) = 4.39 \pm 0.07$  and  $(I-K) = 4.95 \pm 0.09$  for the bright and faint samples, respectively). A two-sided KS test reveals that the probability of the faint colour distribution being drawn from the same population as the bright sample is  $\sim 3 \times 10^{-4}$ . In this comparison we have also chosen to conservatively treat lower limits in  $(I_{814}-K)$  as detections. Since all but two of the non-detections occur in the faint bin (see Fig. 1), objects in the faint sample can only become redder than the values tested. This strengthens the conclusion of a reddening of the fainter EROs. If we completely excise the break region and repeat the test using  $K < 19.0$  (81 objects) and  $K > 19.5$  (86 objects), the trend is unchanged, and the significance only marginally reduced to  $\sim 6 \times 10^{-4}$ .

Thus, the colours of EROs evolve as they pass over the break in the cumulative counts, such that a greater fraction of the faint EROs are redder than their bright counterparts.

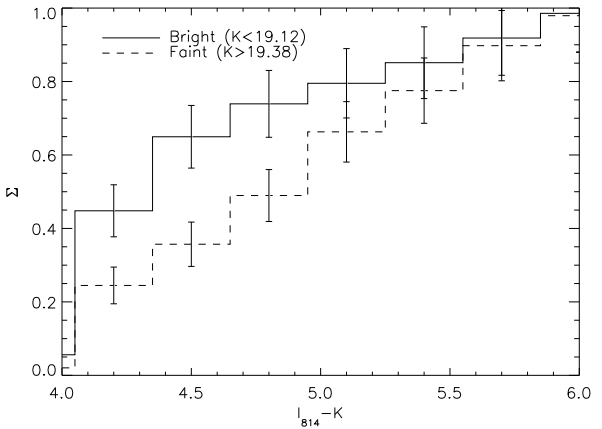


**Figure 5.** A comparison of the cumulative colour distributions of the 100 brightest (solid line) and 100 faintest (broken line) EROs in our sample. Error bars are based on Poisson statistics in each bin. The fainter sample is skewed toward redder colours, indicating that the colour distribution evolves, as galaxies pass over the  $K \sim 19$  break in the number counts.

### 4.2 Evolution of ERO morphologies

We now investigate whether the changes in the colours of EROs across the break in their number counts are mirrored by a change in their morphological mix.

#### 4.2.1 Morphological number counts of EROs

We give the distribution of the different morphological sub-classes of EROs on the colour-magnitude plane in Fig. 6<sup>7</sup>. The main point to note from this plot is that the brightest EROs, which are responsible for the sharp rise in the number counts at  $K \lesssim 19$ , are dominated by galaxies with disk-like morphologies. Indeed at  $K \lesssim 18$ ,  $\gtrsim 80\%$  of the sample are disk systems. To better illustrate the variation in the morphological mix with magnitude we examine the morphologically-classified number counts in Fig. 7. At  $K \sim 18$  bulge systems start to appear, with an even steeper slope than the bright disk population. Merging systems also appear at  $K \sim 18$  and seem to follow the bulge population. To quantify these comparisons, we fit power laws to the morphological subsamples for  $K \leq 19.0$ , where the visual classifications are reasonably complete ( $\sim 90\%$ ), which yields gradients of  $\alpha_{\text{disk}} = 0.77 \pm 0.11$ ;  $\alpha_{\text{bulge}} = 1.17 \pm 0.27$ . For the unclassified (class 0) population:  $\alpha_{\text{unclass}} = 0.57 \pm 0.19$  for  $K \leq 19.0$ , and  $\alpha_{\text{unclass}} = 0.76 \pm 0.40$  for  $19 \leq K \leq 20$ . The remaining classes contain too few objects and/or are not well fit by a power law in this magnitude range.

<sup>7</sup> One particularly bright, red source which is unclassified is ERO198 with  $(I-K) = 6.05 \pm 0.09$  and  $K = 17.87 \pm 0.03$ . This source lies on the edge of a halo from a bright star. It appears to be a genuine detection, and has an F814W counterpart, but its proximity to the star halo *may* bias the magnitudes measured, as the local sky background possesses a large gradient. However, multicolour photometry in additional bands yields a plausible photometric redshift of  $z \sim 1.7$  for this object (see §4.5) and it seems to just be a high redshift, extreme ERO. Note that similar objects are seen in the YT03 data.

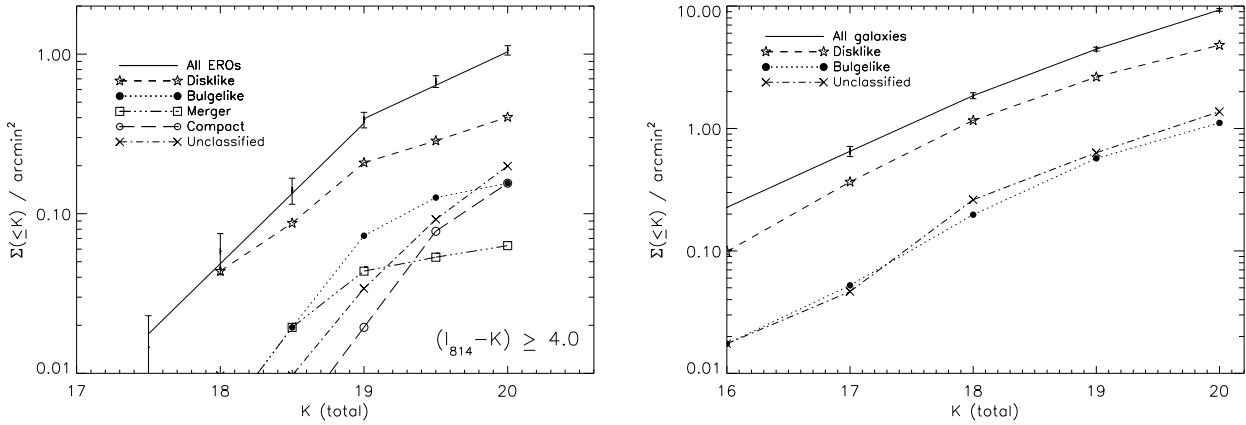


**Figure 7.** Left panel shows the morphological number counts for our data and the double power law fit to the total ERO counts. We do not attempt to correct these counts for incompleteness as a function of morphological type, as this correction is negligible compared with the Poisson uncertainties we assume throughout. Note that nearly all the brightest EROs are disks, and bulges and mergers both appear at  $K \sim 18$ . Right panel shows morphological number counts for *all*  $K$ -selected galaxies using MDS MLE classifications from F814W data.

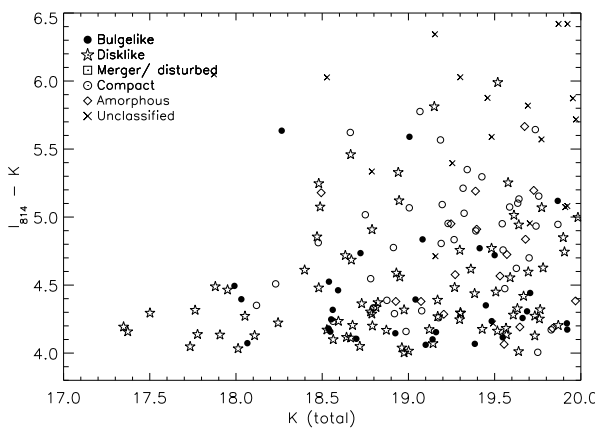


**Figure 6.** The colour-magnitude diagram for the EROs labelled by their visual morphologies. Note the dominance of disk-like morphologies in the brightest EROs in our survey, with bulge systems only starting to appear at  $K > 18$ .

Summarising these results in the scheme of Table 2: to  $K = 20$ , our visual scheme gives  $37 \pm 3\%$  disk-like EROs and  $15 \pm 2\%$  bulge-like, with  $48\%$  not fitting easily into either of these simple classes (19% of which are unclassified). Again, we see around twice as many disks as bulges, but now the unclassified+other fraction is almost twice as high as for the bright subsample. Similarly if we use the MLE classifications, we find that the ratio of bulge to disk galaxies is consistent within the uncertainties with that measured for the bright subsample, but the relative fraction of unclassifiable+other galaxies has doubled.

#### 4.2.2 Comparison with morphological number counts of all $K$ -selected galaxies

We also fit power laws to the  $K$ -selected morphological counts for all galaxies using MDS MLE morphologies from F814W data (Fig. 7). We find slopes of  $\alpha = 0.30 \pm 0.02$  for

the disks and  $\alpha = 0.35 \pm 0.02$  for the bulges, in the range  $18.0 \leq K \leq 20.0$ . The unclassified population follows the bulge counts closely. The counts for these sub-populations are substantially shallower than their counterparts in the ERO sample. Our preferred interpretation of the steepness of the ERO counts is that the EROs are a high redshift ( $z \sim 1$ , inferred from a passively evolved  $M^*$  for the bright EROs of  $K \sim 18$ ) subsample of the total  $K$ -selected galaxy population. We return to the question of redshifts in §4.5.

#### 4.2.3 The nature of the bright disk EROs

To better understand the nature of the bright, ERO disk galaxies we first measure the average semi-major axes of *all* the well-detected disk systems (as measured by SExtractor's `A_IMAGE` parameter). We find a mean of  $\langle A \rangle = (0.16 \pm 0.01)''$ ; while the brighter disk EROs ( $K \leq 18$ ) are also systematically bigger:  $\langle A \rangle = (0.32 \pm 0.03)''$ . Thus these bright (and relatively blue) disk EROs also appear to be larger than the average morphologically-classified disks in the ERO population. Their elongations range from 1.12 to 1.61 with a median of 1.36, suggesting that these systems are only moderately inclined ( $\sim 45^\circ$  to line of sight). If these EROs are at  $z \sim 1$ –2, then the median size of the bright disk sample implies a physical half light radius<sup>8</sup> of  $\sim 3$  kpc, compared to  $\sim 2$  kpc for the full sample of disk EROs. These sizes are comparable to those seen for similarly luminous disk galaxies in the local Universe (e.g. Burgarella et al. 2001). Thus, although these disk EROs are among the brightest and largest galaxies in the sample, they are neither too bright nor too large to be conclusively ruled out as lying at  $z > 1$ . Indeed, recent work has uncovered large disks (with half light radii of 5.0–7.5 kpc) at redshifts  $z = 1.4$ –3.0 (Labbe et al. 2003).

YT03 claimed that around 40% of their disk-like EROs (or one third of all their EROs) showed unusually large, edge on disks and suggest that these systems are actually lower

<sup>8</sup> for all half light radii we use the semi-major axis

redshift contaminants to the  $z \gtrsim 1$  ERO population. We find only one very large edge on disk ERO of comparable size to the one illustrated in YT03's fig. 8 (ERO011 with a half light radius of  $0.45''$ , Fig. 11). Thus we suggest that this contamination is slight for the  $K \leq 20$  ERO population.

#### 4.2.4 ERO sub-populations

Next, we examine the colours and apparent magnitudes of the various morphological sub-populations of EROs in Table 4. We consider the disk-like and bulge-like classes, the unclassified population, the full sample and the amorphous objects (these should be closest to the irregular EROs studied by Moriondo et al. 2000). As would be expected, we see that the median  $K$ -magnitude of the unclassified population is fainter (by  $>0.5$  mag) than any other class. The median colour of the faint sample for the 'all' class is seen to be redder by  $\sim 0.3$  mags than the faint sample. This is the colour evolution reported in §4.1. The median colours of both the bright and faint disks and bulges are consistent. Moriondo et al. (2000) found that irregular EROs were redder than their bulge EROs. We see that our amorphous systems are indeed redder than our bulges, particularly in the bright subsample. We also note that in contrast to the full sample, in this case it is the bright amorphous subsample which is redder than its faint counterpart.

Finally, we briefly examine the environment of the EROs, as defined by the number of  $K \leq 20$  galaxies within 1 arcmin of each ERO. This radius corresponds to a physical size of  $\sim 0.5$  Mpc at  $z \sim 1$ . We failed to find any clear trend, with all morphological types inhabiting similar density environments.

### 4.3 Quantitative evolution of ERO morphologies

In order to quantify the form of this evolution, we artificially faded our bright subsample of EROs to the magnitudes of our faint subsample and statistically compared properties of the artificially faded population with the true faint population. The first quantitative measure we examine is concentration,  $C$  (§3.2.2).

#### 4.3.1 Artificially fading the bright ERO population

To artificially dim the EROs, each of the 100  $K$ -brightest EROs has an  $i814$  magnitude selected randomly from the observed distribution of the 100  $K$ -faintest EROs. Each bright ERO was then extracted from the *HST* image, dimmed to its corresponding faint magnitude (keeping a fixed angular size) and reinserted into a random blank region within the original F814W image. Its concentration was then remeasured. By repeating this for each of the 100 bright EROs, an artificial faint sample is created which can be statistically compared with the true faint sample. By directly fading a bright subsample of our objects, all the uncertainties associated with measuring properties of the faint sample are accounted for. These simulations were repeated 100 times and the maximum probability of the two samples being drawn from the same parent population was found to be 0.6%, with the mean probability of the 100 simulations being 0.1%. Thus, we detect evolution in the concentration indices

for EROs across the break in the ERO number counts. Note that the angular size change over the expected redshift range of the objects is unlikely to be responsible: the angular size of an object only changes by  $\sim 5\%$  between a redshift of 1 and 2. Again, this result still holds if we change the bright and faint samples limits to  $K < 19.0$  and  $K > 19.5$ , although the maximum probability is increased to 14% and the mean is 3%.

#### 4.3.2 Evolution in $\mu - C$ space

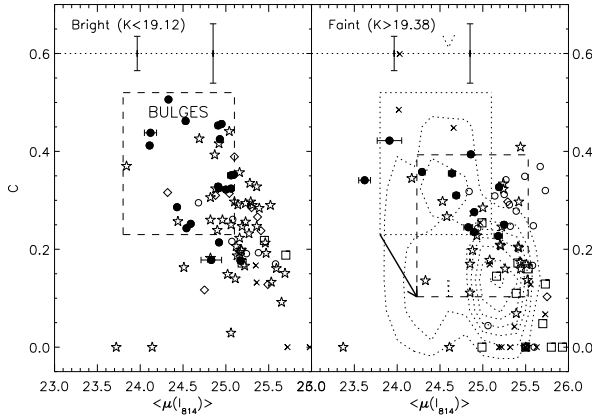
The surface brightness – concentration index ( $\mu - C$ ) classification plane has been used to quantify galaxy morphology, with bulge-dominated galaxies typically residing at higher concentration and greater surface brightnesses than disk-dominated objects (see fig. 1, Abraham et al. 1994).

Fig. 8 shows the distributions for our 100 brightest and 100 faintest EROs. Representative error bars in  $C$  determined from simulations are indicated at the top of each panel and for clarity the errors in surface brightness are shown only for the bulges. The spread of sources in the bright ERO sample is greater than the estimated errors in both quantities, indicating that these quantitative observables are measuring a real variation in the morphological properties within the EROs population, although the distributions for the visually classified bulges and disks overlap significantly. We can identify a region in this plane (described below) towards higher concentration and higher surface brightnesses which contains the bulk of the visually identified bulge-like population. We take the locations of our visually classified bulges and disks in  $\mu - C$  space as further support for the reliability of our visual classifications. In addition, we note that peculiar (i.e. merger and amorphous) systems do not occupy specific areas of the diagram and are scattered throughout all the occupied range.

To test the reliability of the apparent evolution on the  $\mu - C$  plane, we concentrate on the bulge population and perform a simple comparison of the expected numbers of faint, bulge-classified EROs. In the left panel of Fig. 8 we identify a rectangular region which contains a large fraction of the visually identified bulges. We define the completeness and purity of this box as the fraction of bulges out of the total number of bulges (in this sample of 100) located in this box, and the fraction of bulges out of the number of objects within this box, respectively. For the 35 objects in the box in the bright subsample we find a completeness of  $0.76 \pm 0.11$  and a purity of  $0.46 \pm 0.19$ . In the right panel, we move the box by the mean fading vector determined from the simulations, and recalculate these values for the faintest 100 EROs, finding a completeness of  $0.42 \pm 0.16$  and purity of  $0.36 \pm 0.19$  for the 53 objects now in the box. The box selected is quite large and in the bright sample is contaminated by at least as many non-bulges as bulges. However, the translation of this box and the location of visually classified bulges in the faint sample shows that the bulge population behaves as expected, moving along the simulated fading vector, and a comparable fraction of the faint bulge population is still located within this region. We thus conclude that the changing morphological mix between the bright and faint ERO population is not a result of visual misclassification. The contours in the right panel denote the density of artificially faded EROs, the bulk of which lie toward lower

**Table 4.** Average properties of ERO sub-populations. We give the median colours, and median  $K_{Tot}$  magnitude for various morphological sub-populations. Amorphous objects appear significantly redder than the bulge population (particularly in the bright subsample) as noted by Moriondo et al. (2000). Note also that the faint subsample for all morphological types is redder than the bright subsample. This trend is reversed when just considering the amorphous systems. Errors are uncertainties on the median from bootstrap resampling.

Sample	Disks	Bulges	Amorphous	Compact	Merger	Unclassified	All
Median( $I - K$ )							
$K \leq 19.0$	$4.30 \pm 0.05$	$4.40 \pm 0.17$	$5.18 \pm 0.31$	$4.19 \pm 0.08$	$4.58 \pm 0.22$	$6.68 \pm 0.41$	$4.38 \pm 0.05$
$19.0 \leq K \leq 20.0$	$4.41 \pm 0.10$	$4.40 \pm 0.12$	$4.73 \pm 0.20$	$4.29 \pm 0.17$	$4.57 \pm 0.13$	$5.54 \pm 0.10$	$4.71 \pm 0.08$
#/%							
$K \leq 19.0$	43/53.75%	15/18.75%	2/2.50%	4/5.00%	9/11.25%	7/8.75%	80/100%
$19.0 \leq K \leq 20.0$	41/28.47%	18/12.50%	16/11.11%	28/19.44%	5/3.47%	36/25.00%	144/100%
Median( $K_{Tot}$ )	$18.97 \pm 0.12$	$19.04 \pm 0.18$	$19.56 \pm 0.08$	$19.54 \pm 0.12$	$18.91 \pm 0.18$	$19.63 \pm 0.10$	$19.27 \pm 0.06$



**Figure 8.** The distribution of mean  $i_{814}$  surface brightness ( $\mu$ ) versus concentration index ( $C$ ) for the 100 brightest (left panel) and 100 faintest (right panel) EROs in our survey. Symbols denote visual morphologies and are the same as for Fig. 6. The uncertainty in  $\mu$  is just shown on bulge classes for clarity and the typical errors in  $C$  estimated from simulations are shown at top of each plot. The box in the left panel is the region selected to contain a large fraction of visually identified bulges ( $\sim 70\%$ ). The arrow in the right panel indicates the translation in  $\mu - C$  observed when the bright ERO population is faded to match the faint population (as described in text) and the dashed box shows the movement of the translated classification box. Contours in the right panel show the density of artificially faded galaxies (of all morphological types). It appears that the distribution of the simulated faded population extends to lower  $C$  than is seen in the real faint sample, suggesting that the low- $C$  galaxies seen in the bright sample are absent in the fainter population.

values of  $C$  than seen in the real faint sample (as measured in § 4.3.1).

Hence, it would appear that morphological changes are associated with a decline in the number of low concentration objects. Galaxies in this region of the  $\mu - C$  plane appear to be disks in the bright sample (and would be expected to be disks in the local universe, e.g. Abraham et al. 1994). Thus we interpret the break in the ERO counts as a real decrease in the number of disk-like galaxies in the population at  $K \gtrsim 19$ .

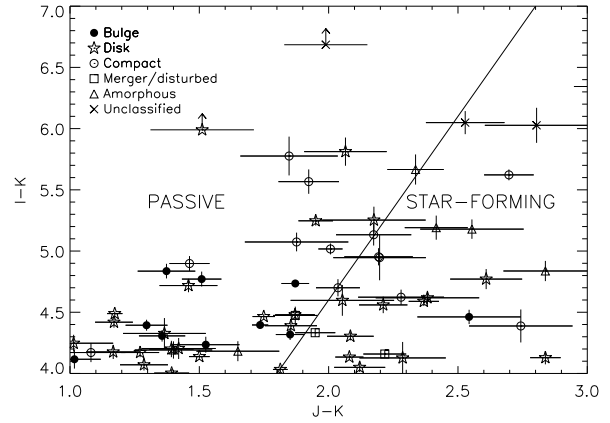


**Figure 9.** The  $(I_{814} - K)$  versus  $(J - K)$  colour-colour diagram for subsample of our EROs with  $J$ -band photometry. EROs are labelled with their visual classifications. The solid line shows the proposed division between photometrically classified passive and star-forming galaxies (Pozzetti & Mannucci 2000). This division is broadly supported by our morphological classifications, however a number of EROs with disk-like morphologies appear in the lower left corner and hence fall in the elliptical category. As we show in §4.4, a more detailed modelling of the SEDs of these galaxies suggests that they are star-forming galaxies which this simple photometric classification scheme is failing to correctly identify.

#### 4.4 Photometric classification of EROs

Another possibility for distinguishing evolution in the various subclasses of EROs is multicolour photometry. Pozzetti & Mannucci (2000) proposed a photometric classification scheme for separating dusty star-forming SEDs from passive systems in the  $I/J/K$  colour plane. Using the subsample of our survey with  $J$ -band photometry we illustrate this in Fig. 9. The solid line denotes the Pozzetti & Mannucci (2000) division between the bluer, passive and redder, star-forming systems. We can compare this classification scheme with the distribution of our visual morphological classifications to test the extent of the overlap between these two approaches. Here we start from the naive assumption that all morphologically-classified bulge systems will have passive SEDs, while any galaxy with a disk component is probably an ERO by virtue of a strong dust component produced by ongoing star formation activity.

51 EROs lie in the passive region of Fig. 9, and 21 in the star-forming region. Firstly we quantify the fractions of photometrically classified objects in each morphological class. Of the 30 disks, 21 (70%) are classified as having star-forming SEDs, with only 9 (30%) falling into the passive region. Equally, 10 (91%) of the 11 bulges are classed as passive and 11 (78.6%) of the 14 compact sources have colours consistent with passive SEDs. For the remaining classes, 2 (66%) of the 3 mergers; 3 (50%) of the 6 amorphous and 6 (60%) of the 10 unclassified objects have SEDs classed as star-forming.

Thus the photometric classifications crudely support our prejudices based on the morphologies of the EROs: most disk systems have star-forming SEDs and most bulge systems have passive colours; indeed we find only one morphologically-classified bulge lies in the star-forming region. The main discrepancy comes from a number of disks falling into the passive region of the plot, although these are mostly relatively blue in  $(I_{814} - K)$ , with  $(I_{814} - K) \lesssim 4.5$ . Closer inspection of the morphologies of these EROs does not show strong evidence of them being early-type disk galaxies (which could be expected to show passive SEDs).

Another clear trend from this comparison is that a similar fraction of compact sources are classed as passive to that seen for the bulge population. This is consistent with the idea that the compact class comprises bulge systems which are too faint to be unambiguously classified as such. The amorphous, merging and unclassified samples show much higher proportions of sources with star-forming SEDs, suggesting that these indeed represent morphologically more complex systems, rather than misclassified faint bulges.

Hence using our visual morphologies we find good agreement with the photometric scheme of Pozzetti & Mannucci (2000) for the higher signal to noise bulge-classified galaxies and less agreement for the disk-classified ERO sample. We use this to infer the probable morphological mix of the lower signal to noise amorphous and compact EROs, associating the amorphous systems with star-forming and the compact systems as mostly passive.

S02 used the equivalent  $R/J/K$  colour-colour diagram to analyse the colours of radio-detected and undetected EROs. They found a similar level of agreement, in that the EROs expected on the basis of their radio emission to be star-forming mainly fell into the star-forming region of the diagram, with some cross-contamination. Smith et al. (2002a) also used this colour-colour diagram to examine the location of their *HST* imaged EROs. They found that all their objects with compact morphologies lay within the passive region. The size of their  $J$ -band photometric errors prevented them from drawing conclusions from their irregular objects. An alternative but similar colour selection criterion in  $(I - J) - (J - K)$  colour-colour space was used by Wehner et al. (2002) to study the colours of EROs with sub-mm observations. They found that objects in the star-forming region of the diagram were indeed responsible for the bulk of the 850 $\mu$ m emission detected from their coadded observations, indicative of dusty star-formation activity. Roche et al. (2003) adopted a similar scheme using galaxy tracks plotted in  $I/J/H/K$  colour space to attempt to separate the classes. They noted, as with these other works, that a large fraction of the EROs lie close to the dividing line between classes. This could be symptomatic of the size of the

photometric errors, or indicate that most of this class of object do indeed possess SEDs intermediate between dusty star-forming and passive stellar populations.

#### 4.5 Photometric Redshifts

22 of our ERO sample have good detections in four photometric bands:  $R_{606}$  and  $I_{814}$  from the MDS observations and  $J$  and  $K$  from our INGRID survey. The MDS F606W observations of these fields were retrieved from the ST-ECF archive and reduced in a similar manner to the F814W images (§2.2). For these galaxies it is possible to investigate the properties of their SEDs in more detail. However, the apparent colours are affected both by their intrinsic SED and their redshift and we are therefore required to fit for both of these variables. Hence, we have used a photometric redshift code, HYPERZ (Bolzonella et al. 2000), to study these objects. We adopted a procedure similar to S02. We attempt to fit, in turn, a dusty star-forming and an evolved SED to each object. We use a single star-formation history with an e-folding time-scale of  $\tau = 1\text{Gyr}$ , a Miller-Scalo IMF and solar metallicity. The dusty SED is allowed reddening values in the range  $A_V = 1 - 6$  (consistent with values estimated by Cimatti et al. 2002), and the evolved SED must have a reddening value  $A_V \leq 0.2$ . Redshifts in the range 0 to 4 are considered. We list the photometric data and the derived properties for this sample in Table 5. In this analysis we retain the F606W passband, rather than introducing any uncertainty by transforming it to another, more common, filter system. We consider only the EROs with *detections* in all four passbands, rather than including limits as well, as using three or fewer detections leads to very poorly constrained SEDs. If this selection introduces any bias, it will be that requiring detections in the optical passbands preferentially selects bluer galaxies. However, we are primarily interested in the relation between SED classifications and colour/morphological classifications, rather than constructing a fair sample.

From the 22 EROs, 14 could be fit using HYPERZ; the remaining 8 are typically the reddest objects in  $(F606W - K)$ . All but one have  $(F606W - K) \gtrsim 7$ . The median redshift of our sample with photometric redshifts, which has a median magnitude of  $K = 19.43 \pm 0.19$ , is  $z = 1.20 \pm 0.22$  with all but two EROs predicted to lie in the range 0.7 to 1.8. Cimatti et al. (2002) found a median redshift of  $\langle z \rangle = 1.1 \pm 0.2$  with galaxies in the range  $z = 0.7 - 1.4$ , for  $(R - K) \geq 5.0$ ,  $K \leq 19.2$  EROs, using optical spectroscopy. Thus our sample spans the same redshift range as that of Cimatti et al. (2002), but with a higher upper limit, as might be expected from the fainter magnitude range probed here.

For the fitted EROs we find 11/14 have disk-like morphologies, with a further 2/14 either amorphous or LSB and one unclassified (the high fraction of morphologically-classified EROs in this relatively faint  $K$ -band subsample simply reflects our selection of EROs with strong optical detections).

The photometric classifications give a dusty star-forming SED as the best fit for all but two cases which favour evolved SEDs. Interestingly, half of these EROs (7/14) with dusty star-forming SEDs lie in the passive region of the  $(I_{814} - K) - (J - K)$  plane (Fig. 9), with many of the EROs

occupying the  $(I_{814} - K) \sim 4.0$  region in the lower left corner of the diagram. This may reflect our selection, where by requiring the EROs be red in  $(I - K)$  but sufficiently blue to be well detected in  $I_{814}$  and F606W, we select unusual systems, possessing strong UV upturns and possibly a mixture of young and evolved stellar populations. We note that of the blue disks in the passive region, 29% (2/7, or 2/9 if we include two borderline passive cases) are best fitted with evolved SEDs, suggesting that these are indeed passive disk systems.

One of these EROs (#226, an amorphous object) is best-fitted as a low-luminosity, dusty system at low redshift ( $z \lesssim 0.4$ ), but this is only marginally favoured over an evolved SED at  $z=1.2$ . Overall, it seems unlikely that a large fraction of our EROs are at such low redshifts ( $z \sim 0.4$ ). Moreover, such systems are not seen in the brighter Cimatti et al. (2002) spectroscopic sample.

#### 4.6 High-redshift EROs

One of the EROs in the photometric analysis in the previous section has a much higher estimated redshift than the remainder of the sample. This ERO is #158 at  $z_{phot} = 3.39_{-0.26}^{+0.11}$ . This source is one of only two EROs in this subsample with  $(J - K) \geq 2.3$ . Van Dokkum et al. 2003 (see also Franx et al. 2003) have recently shown through optical spectroscopy that selecting galaxies with  $(J - K) \geq 2.3$  efficiently selects objects with a prominent optical break (either the 3625Å Balmer break or the 4000Å CaII H+K break) at  $z \geq 2$ . We can use all of our MDS fields with  $I/J/K$  photometry (81 arcmin<sup>2</sup>) to examine the nature of this class of ERO. Adopting this selection, we find 24 EROs with  $(J - K) \geq 2.3$ , or a surface density of  $(0.30 \pm 0.06)$  arcmin<sup>-2</sup> (Poisson error) to  $K \leq 20$ . Van Dokkum et al. 2003 only give the surface density at  $K = 21$  ( $1.09_{-0.16}^{+0.20}$ ) and so we are unable to compare with their numbers, except to note that our surface density is lower to this brighter magnitude limit, and that there are very large field to field variations in this class of ERO (there are *no*  $(J - K) \geq 2.3$  EROs in the HDFS, van Dokkum et al. 2003). The morphological mix of these galaxies is  $20 \pm 9\%$  disk-like,  $4 \pm 4\%$  bulge-like,  $17 \pm 7\%$  amorphous,  $8 \pm 6\%$  merger,  $13 \pm 7\%$  compact and  $38 \pm 13\%$  unclassifiable. The fraction of bulges relative to disks in the sample is lower than for the full  $(I - K) \geq 4.0$  ERO sample, although just compatible within the 1- $\sigma$  Poisson errors. The fraction of peculiar (not disk-like or bulge-like) EROs is higher than for the full sample. The magnitudes of these  $(J - K) \geq 2.3$  selected EROs span the full range of the  $(I - K)$  ERO sample. It is interesting to note the lack of bulge-like systems in this perhaps higher redshift sample, and also the absence of passive spectra from van Dokkum et al. (2003)'s sample. This could be an indication that at these redshifts ( $z \gtrsim 2$ ) the formation epoch of early type galaxies is being approached (as suggested by complimentary studies of cluster ellipticals, e.g. Stanford et al. 1998).

#### 4.7 ERO sample differences in different photometric passbands

A range of different photometric criteria have been used to identify 'Extremely Red Objects'. How do the different criteria affect the mix of objects selected? The ERO number

counts for samples selected by a variety of definitions (e.g.  $(R - K) \geq 5.3$ ,  $(I - H) \geq 3.0$ ) are in broad agreement (e.g. fig. 7 of YT03), and in addition the  $K \approx 19$ –20 break in the counts is seen in sufficiently deep data selected by  $(I_{814} - K)$ ,  $(I - H)$ , and  $(R_{702} - K)$  (this work; McCarthy et al. 2001; Smith et al. 2002a, respectively). However, a direct comparison of the details of the samples such as the relative morphological mixes of EROs using different colour selection has yet to be addressed.

The difference between the  $(R - K)$  and  $(I - K)$  colour cuts can be examined for a subsample of our ERO sample with F606W data. F606W can be approximately transformed to the Cousins  $R$  passband using  $R_{606} \approx F606W_{Vega} - 0.37(F606W - F814W)_{Vega}$  (Metcalfe et al. 2001). This results in 27 EROs with measurable  $R_{606}$  photometry (Fig. 10). Only three of the  $(I_{814} - K)$  selected EROs are bluer in  $(R_{606} - K)$  than the typical selection criterion of  $(R_{606} - K) \geq 5.3$ . One of these sources is very close to the selection boundary and would be found using the  $(R_{606} - K) \geq 5.0$  criterion (e.g. Cimatti et al. 2002), and may even be found with the former criterion, given the uncertainty in the F606W to  $R_{606}$  transformation. The remaining two EROs have  $(R_{606} - K) \sim 4.0$  and would not. Thus,  $\approx 90\%$  of our EROs would also be selected in an  $(R_{606} - K)$  ERO survey (in agreement with S02 who found a value of 93%), suggesting that  $(I_{814} - K) \geq 4.0$  is a less stringent ERO requirement than  $(R_{606} - K) \geq 5.3$ . Furthermore, for this admittedly small sample, all the galaxies dropping out of the ERO category when selected in  $(R - K)$  are disks, which supports the suggestion by YT03 that  $(I - K)$  selected ERO surveys may preferentially include disks. To quantitatively compare the different morphological mixes found by the two techniques requires  $R$  and  $I$  band data and *HST* morphologies on the same regions of sky (e.g. Gilbank et al. in prep).

We also performed visual classifications of the EROs in F606W to compare with the morphologies derived from the F814W images. We find for the 27 EROs with sufficient signal for F606W photometry: 8 of these are too faint to morphologically classify; 10 of these are disk-like in F606W and were also disk-like in F814W; 2 galaxies were compact and disk-like in F814W and were simply compact in F606W; 5 galaxies appear LSB and disturbed in F606W whereas these systems were just classed as disk-like in F814W; one galaxy appears amorphous in F606W and disk-like in F814W. One ERO classed as compact and disk-like in F606W was classed as compact and symmetrical in F814W (nominally a bulge class). This represents the only discrepancy between our notional bulge and disk classes, but the difference is slight as in both passbands the object is compact and symmetric. Thus, the agreement between the F814W and F606W visual morphologies is very good. There is a tendency for the disks in the latter to exhibit more disturbed morphologies, as would be expected as the F606W probes further into the extreme ultraviolet, in each EROs' rest-frame. This agreement between passbands is reassuring, as F606W at  $z \sim 1.0$  corresponds to the same rest-frame wavelength as F814W at  $z \sim 1.5$  – a plausible redshift spread for the ERO sample. For this small subsample, we only find one (marginal) bulge – disk misclassification, whereas we assume Poisson uncertainties on all our measured fractions throughout this work.

**Table 5.** Photometric properties of EROs with F606W,  $I_{814}$ ,  $J$  and  $K$  data. In the SED fitting procedure, the raw F606W magnitudes have been used directly instead of attempting to convert to  $R_{606}$ . <sup>a</sup> – best fitting SED type: D – dusty; E – evolved. <sup>b</sup> – PM00 shows the classification based on the Pozzetti & Mannucci scheme. P – passive, S – star-forming. Square brackets indicate systems close to the dividing line, whose errors allow them into the other class. <sup>c</sup> – the 99% confidence interval for the photometric redshift. <sup>d</sup> – morphology refers to visual classification.

ID	(F606W– $K$ )	( $I_{814}$ – $K$ )	( $J$ – $K$ )	$K$	SED <sup>a</sup>	PM00 <sup>b</sup>	$z_{phot}$ (99%) <sup>c</sup>	$z_{phot}$	Morph <sup>d</sup>	Comments (visual morphology)
001	6.93± 0.14	4.60± 0.13	2.05± 0.22	19.69	D	[S]	1.20	0.28–1.49	2	
002	6.62± 0.13	4.33± 0.13	1.37± 0.16	19.63	D	P	1.18	0.93–1.51	2	early-type?
158	5.78± 0.06	4.13± 0.05	2.84± 0.06	18.11	D	S	3.86	3.20–4.00	6	edge-on late-type disk
167	6.04± 0.14	4.13± 0.13	2.29± 0.17	19.73	D	P	0.71	0.15–1.26	6	small edge-on disk 1''/ late-type
197	5.66± 0.09	4.20± 0.09	1.42± 0.14	19.87	D	S	1.49	1.26–1.79	2	
198	8.78± 0.23	6.05± 0.09	2.53± 0.15	17.87	D	[S]	1.71	0.83–1.93	0	
204	7.27± 0.17	5.25± 0.11	2.17± 0.23	19.58	D	[P]	1.00	0.95–1.9	2	
206	7.27± 0.05	4.30± 0.03	2.08± 0.09	18.78	D	S	0.89	0.58–1.18	6	edge-on Scd/Sdm 2.5'' (near chip edge)
209	8.42± 0.10	5.25± 0.04	1.95± 0.07	18.48	D	[P]	1.49	1.44–1.66	2	
224	5.77± 0.07	4.18± 0.06	1.17± 0.10	19.43	D	P	1.49	1.34–1.61	6	edge-on disk with tidal tail/cmp 2''
225	6.18± 0.05	4.17± 0.04	1.27± 0.07	18.53	E	P	1.09	1.00–1.10	6	face-on asymm disk 1.5''
226	5.84± 0.08	4.19± 0.07	1.40± 0.15	19.65	D	P	0.10	0.00–0.42	9	
227	5.97± 0.07	4.72± 0.05	1.46± 0.11	18.63	D	P	1.79	1.51–2.00	5	face-on disk or clumpy LSB
229	6.09± 0.06	4.07± 0.05	1.29± 0.09	19.14	E	P	1.06	0.97–1.09	6	late-type slightly inclined disk 2''

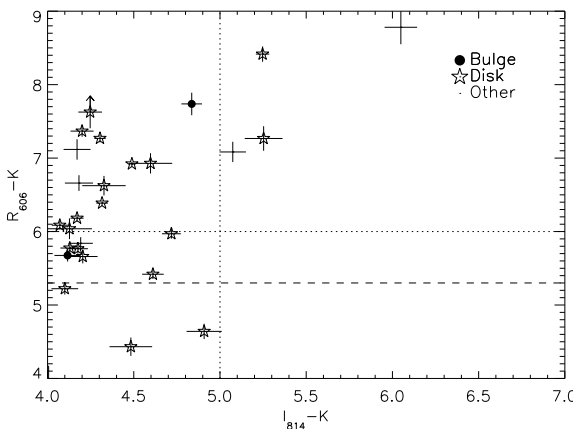


**Figure 10.** The  $(R_{606} - K) - (I_{814} - K)$  colour-colour diagram for our ERO sample (selected by  $(I_{814} - K) \geq 4.0$ ) with available F606W photometry. The dashed line shows the typical  $(R_{606} - K) \geq 5.3$  selection bound for  $R$ -selected EROs, and the redder  $(R_{606} - K) \geq 6.0$  limit discussed in the text. Points are labelled according to their visual morphologies in broad classes – disk-like, bulge-like, or unclassified. Vertical error bars represent only the error in the F606W photometry and do not account for the uncertainty in the transformation to  $R_{606}$ . This suggests that the  $(I_{814} - K) \geq 4.0$  selection criterion is less stringent than  $(R_{606} - K) \geq 5.3$ .

#### 4.8 Composition of the ERO population

Our visual and quantitative analysis of the morphological mix of our ERO catalogue suggests that the ERO population at  $K \leq 19$  is dominated by galaxies with disk-like morphologies (54% of the total sample), with EROs with bulge-like or compact morphologies making up around a fur-

ther quarter and a modest fraction ( $\sim 15\%$ ) of EROs with disturbed, merging or amorphous morphologies. As we have shown, this distribution is similar to that found by previous studies (YT03; Smith et al. 2002a). In contrast, our faint ERO subsample, with  $K = 19\text{--}20$ , has a lower fraction of disk-like EROs, down to less than a third, with the fractions of the other classes effectively unchanged and the decline in the disk-like EROs being made up for by a corresponding increase in the fraction of those with amorphous, merger or unclassified morphologies. Our quantitative tests of this evolution confirm that the apparent decline in the disk-like fraction is real and is not due to our inability to classify faint examples of this population.

We can now ask what limits we can place on the proportion of the ERO population arising from galaxies which are red due to dust-obscuration and what fraction comes from evolved, passive systems. We use our visual classifications to divide our sample into star-forming or passive EROs by taking extreme values in the following way. We assume that the minimum fraction of star-forming EROs is given by all the disk-like galaxies (although note that passive disks are also likely, § 4.5; Smith et al. 2002b), and the maximum star-forming fraction is given by all the galaxies which could plausibly harbour star-formation (including the disks, amorphous, mergers and *all* the unclassified objects). In the same way we associate all bulge-like EROs with passive systems and add all compact and unclassified sources to this to generate an upper limit. We thus find 54–77% star-forming and 19–31% passive EROs in the bright subsample ( $K \leq 19.0$ ), and 29–71% star-forming and 13–58% passive in the faint sample ( $19.0 \leq K \leq 20.0$ ). For the full sample these numbers are 38–73% and 15–48% for star-forming and passive EROs, respectively. S02 (based on an ERO sample selected using  $(R - K) \geq 5.3$ ) used deep radio data to estimate the

fraction of star forming EROs, finding a value of  $\sim 45\%$ , to  $K = 20.5$ . This is compatible with our estimate based on morphologies. Furthermore, they used photometric SED fitting to assess the fraction of dusty galaxies, placed a firm lower limit of  $\geq 30\%$ , and estimated that possibly  $60 \pm 15\%$  of this ERO population could be dusty star-forming galaxies. Again, this does not contradict our findings.

In the discussion above, it is the increasing fraction of morphologically unclassified EROs in the faintest samples which produces the greatest uncertainty in the evolutionary trends we derive. These galaxies make up a quarter of the  $K = 19\text{--}20$  sample and appear to also be responsible for the reddening of the whole ERO population at  $K \gtrsim 19$ , especially when balanced against the declining fraction of bluer, disk-like EROs (Table 4). It is tempting to associate this population with the counterparts to the dusty, active sources selected in the sub-mm waveband (e.g. Smail et al. 2002a; Wehner et al. 2002). However, the confirmation of this will have to await complimentary multiwavelength and morphological studies, with the latter either benefiting from the higher red sensitivity of the new ACS camera on-board *HST* and the revival of the NICMOS near-infrared imaging capability of *HST*.

#### 4.9 Cosmological significance of EROs

Assuming the median photometric redshift ( $z \sim 1.5$ ) for our sample, the break around  $K = 19$  corresponds to a luminosity of  $M_V \sim -19.7$ . For the star-forming population, we correct this value for reddening to give  $M_V \sim -22.1$  (assuming  $A_V \sim 2.4$ , Cimatti et al. 2002). This unobscured luminosity corresponds approximately to an  $L_V^*$  galaxy today. Conservatively assuming no further star-formation activity in these galaxies between  $z \sim 1.5$  and the present day (and no substantial merging), these galaxies would actually correspond to sub- $L_V^*$  galaxies at  $z = 0$ . Similarly, if we adopt passive evolution models for the passive/bulge population, then  $K = 19$  at  $z \sim 1.5$  corresponds to an  $L_V^*$  elliptical today.

Taking the range of our photometric redshifts ( $0.7 \leq z \leq 1.8$ , ignoring the two outliers) we derive a comoving volume for our survey of  $\sim 2 \times 10^5 \text{ Mpc}^{-3}$ . This gives a space density for our full ERO sample of  $\sim 1 \times 10^{-3} \text{ Mpc}^{-3}$ . This is only a crude estimate since we do not know the true redshift distributions of the galaxies, and furthermore, the redshift distributions of the dusty star-forming and passive EROs are unlikely to be the same. Thus we use only an order of magnitude estimate. This number density agrees to this level with that derived locally from SDSS+2MASS data for  $\geq L^*$  galaxies (Bell et al. 2003). Thus, the ERO population could plausibly account for a sizable fraction ( $\gtrsim 10\%$ , and potentially all) of the stars seen in luminous ( $\sim L^*$ ) galaxies locally.

A more detailed comparison of the ERO counts with a variety of evolution models was undertaken by Smith et al. (2002a), who compared their ERO counts with Pure Luminosity Evolution (PLE) and semi-analytic hierarchical galaxy formation models. The only model to correctly reproduce the cumulative ERO number counts was one in which the ERO population was modelled as a single population of passive galaxies. This model now clearly overestimates the number of passive EROs as we have been shown that a siz-

able fraction of the EROs are not simple passive systems. The more realistic models examined by Smith et al. (2002a) – PLE with a mixture of galaxy types and semi-analytic galaxy formation models – both under-predicted the number of EROs by around an order of magnitude. A comparison with these models is beyond the scope of this paper and will be presented in future work. However, we note briefly that more recent semi-analytic models, which include bursts of star formation at high redshift absent in the Cole et al. (2000) reference model, now reproduce the number counts for  $(I - K) \geq 4.0$  EROs (C. Baugh, priv. comm.). Unfortunately, the numbers of objects in redder subsamples (e.g.  $(I - K) \geq 5.0$ ) are still underestimated by around an order of magnitude. The requirement of these starbursts at higher redshift (which is also indicated by the presence of luminous, passive galaxies at  $z \sim 1$ ) is consistent with the interpretation of SCUBA sources as protoelliptical galaxies in the process of formation (e.g. Smail et al. 2002a).

## 5 CONCLUSIONS

We have compiled a new catalogue of  $K$ -selected Extremely Red Objects in regions with deep *HST*  $I_{814}$ -band observations. We apply a number of tests to examine the nature of the ERO population and investigate the origin of the turnover in the ERO number counts around  $K \sim 19$ . The main aim of our work is to study the morphologies of our EROs using the exquisite resolution of the *HST*. However, for a subsample of our dataset with multicolour data we can also utilise SED-fitting as a classification tool. Hence, we were able to examine the commonly applied hypothesis that the passive population defined by multicolour photometry (or equally spectral line diagnostics) is associated with bulge-dominated morphologies; and that EROs with the colours of dusty star-forming galaxies have disk-like/irregular morphologies.

1. We find a surface density of  $(I_{814} - K) \geq 4.0$  EROs  $(1.14 \pm 0.08) \text{ arcmin}^{-2}$  at  $K = 20.0$ . The number count slope flattens from  $\alpha = 0.88 \pm 0.09$  for  $K \leq 19.0$  to  $\alpha = 0.42 \pm 0.19$  for  $19.0 \leq K \leq 20.0$ , in good agreement with other surveys in the literature.

2. This turnover in the number counts is associated with a reddening of the faint ERO population, from a median colour of  $(I_{814} - K) = 4.38 \pm 0.05$  at  $K \leq 19.0$  to  $(I_{814} - K) = 4.71 \pm 0.08$  at  $19.0 \leq K \leq 20.0$ .

3. Our visual morphological fractions at the bright end ( $K \leq 19.0$ ) are in good agreement with Yan & Thompson (2003), and we extend this sample to fainter depths, finding a mix of 35% disk-like, 15% disturbed/irregular, 30% spheroidal or compact and 20% unclassifiable.

4. Using quantitative measures, we find that the concentrations of EROs evolves across the break in their number counts, such that the fraction of disk-like galaxies declines.

5. We find on the basis of  $I/J/K$  colours, using the scheme of Pozzetti & Mannucci (2000), that most disk-like and amorphous galaxies are associated with dusty star-formation activity, and most bulge-like and compact sources have the colours of passive stellar populations. However,  $\sim 30\%$  of disks appear to have the colours of passive stellar populations. These are probably genuinely passive disks or at least have substantial evolved stellar populations.

6. We also fit the SEDs of our EROs finding slightly better agreement between the morphological classification and the expected star-formation activity of such morphological types, than the Pozzetti & Mannucci (2000) classification, i.e. most disk-like EROs exhibit photometric signs of recent star-formation.

7. For a subsample of our EROs we derive SED-fitted photometric redshift distributions with a median of  $z = 1.20 \pm 0.22$ , in reasonable agreement with spectroscopic redshifts of small samples of somewhat brighter EROs.

We have highlighted the diversity of Extremely Red Objects, comparing morphological and photometric classification schemes. We suggest that the apparent break in ERO counts at  $K \sim 19$  is due to a rapid rise in bluer disk EROs at bright magnitudes. The dominance of this population declines as it is joined around  $K \sim 18.5$  by a more modestly increasing population of galaxies comprising bulges, amorphous, merging and increasingly unclassifiable systems. We have shown that these blue disk EROs have properties not inconsistent with them being at the same redshifts as the rest of the other ERO sub-populations.

The next steps in understanding the nature of the ERO population are: spectroscopic follow up of a large sample of faint EROs (building on the initial work of Cimatti et al. 2002 at brighter magnitudes) in order to obtain star formation rates, extinction values and redshift distributions (particularly to understand the bluer disk-like EROs); and a detailed comparison with semi-analytic and other galaxy formation models.

## ACKNOWLEDGMENTS

We thank the referee for useful suggestions which improved the structure and content of this manuscript. We thank Carlton Baugh, Richard Bower, Malcolm Currie, John Lucey, Nigel Metcalfe and Mark Sullivan for helpful discussions and comments, and also the ST-ECF staff for providing an excellent service in the WFPC2 associations archive. We are particularly grateful to Peter Draper for technical assistance with the CCDPACK software, and for his expertise with world coordinate systems. DGG acknowledges support from the Leverhulme Trust. IRS acknowledges support from the Royal Society and Leverhulme Trust.

## REFERENCES

Abraham, R. G., Tanvir, N. R., Santiago, B. X., Ellis, R. S., Glazebrook, K., & van den Bergh, S. 1996a, MNRAS, 279, L47

Abraham, R. G., Valdes, F., Yee, H. K. C., & van den Bergh, S. 1994, ApJ, 432, 75

Abraham, R. G., van den Bergh, S., Glazebrook, K., Ellis, R. S., Santiago, B. X., Surma, P., & Griffiths, R. E. 1996b, ApJS, 107, 1

Bell, E. F., McIntosh, D. H., Katz, N., & Weinberg, M. D. 2003, ArXiv Astrophysics e-prints, 2543

Bertin, E. & Arnouts, S. 1996, A&AS, 117, 393

Bolzonella, M., Miralles, J.-M., & Pelló, R. 2000, A&A, 363, 476

Burgarella, D., Buat, V., Donas, J., Milliard, B., & Chapelon, S. 2001, A&A, 369, 421

Cimatti, A., Daddi, E., Mignoli, M., Pozzetti, L., Renzini, A., Zamorani, G., Broadhurst, T., Fontana, A., et al., 2002, A&A, 381, L68

Cole, S., Lacey, C. G., Baugh, C. M., & Frenk, C. S. 2000, MNRAS, 319, 168

Cowie, L. L., Gardner, J. P., Lilly, S. J., & McLean, I. 1990, ApJ, 360, L1

Daddi, E., Cimatti, A., Pozzetti, L., Hoekstra, H., Röttgering, H. J. A., Renzini, A., Zamorani, G., & Mannucci, F. 2000, A&A, 361, 535

Dey, A., Graham, J. R., Ivison, R. J., Smail, I., Wright, G. S., & Liu, M. C. 1999, ApJ, 519, 610

Dunlop, J., Peacock, J., Spinrad, H., Dey, A., Jimenez, R., Stern, D., & Windhorst, R. 1996, Nature, 381, 581

Firth, A. E., Somerville, R. S., McMahon, R. G., Lahav, O., Ellis, R. S., Sabbey, C. N., McCarthy, P. J., Chen, H.-W., et al., 2002, MNRAS, 332, 617

Franx, M., Labbé, I., Rudnick, G., van Dokkum, P. G., Daddi, E., Förster Schreiber, N. M., Moorwood, A., Rix, H., Röttgering, et al., 2003, ApJ, 587, L79

Griffiths, R. E., Ratnatunga, K. U., Neuschaefer, L. W., Casertano, S., Im, M., Wyckoff, E. W., Ellis, R. S., Gilmore, G. F., Elson, R. A. W., Glazebrook, K., Schade, D. J., Windhorst, R. A., Schmidtke, P., Gordon, J., Pascale, S. M., Illingworth, G. D., Koo, D. C., Bershadsky, M. A., Forbes, D. A., Phillips, A. C., Green, R. F., Sarajedini, V., Huchra, J. P., & Tyson, J. A. 1994, ApJ, 437, 67

Hawarden, T. G., Leggett, S. K., Letawsky, M. B., Ballantyne, D. R., & Casali, M. M. 2001, MNRAS, 325, 563

Holtzman, J. A., Burrows, C. J., Casertano, S., Hester, J. J., Trauger, J. T., Watson, A. M., & Worthey, G. 1995, PASP, 107, 1065

Labbe, I., Rudnick, G., Franx, M., Daddi, E., van Dokkum, P. G., Schreiber, N. M. F., Kuijken, K., Moorwood, A., et al., 2003, astro-ph/0306062

Lilly, S. J., Cowie, L. L., & Gardner, J. P. 1991, ApJ, 369, 79

Mannucci, F., Pozzetti, L., Thompson, D., Oliva, E., Baffa, C., Comoretto, G., Gennari, S., & Lisi, F. 2002, MNRAS, 329, L57

McCarthy, P. J., Carlberg, R. G., Chen, H.-W., Marzke, R. O., Firth, A. E., Ellis, R. S., Persson, S. E., McMahon, R. G., et al., 2001, ApJ, 560, L131

Menanteau, F., Ellis, R. S., Abraham, R. G., Barger, A. J., & Cowie, L. L. 1999, MNRAS, 309, 208

Metcalfe, N., Shanks, T., Campos, A., McCracken, H. J., & Fong, R. 2001, MNRAS, 323, 795

Mink, D. J. 1997, in ASP Conf. Ser. 125: Astronomical Data Analysis Software and Systems VI, Vol. 6, 249–+

Mohan, N. R., Cimatti, A., Röttgering, H. J. A., Andreani, P., Severgnini, P., Tilanus, R. P. J., Carilli, C. L., & Stanford, S. A. 2002, A&A, 383, 440

Monet, D. G. 1998, American Astronomical Society Meeting, 30, 1427

Moriondo, G., Cimatti, A., & Daddi, E. 2000, A&A, 364, 26

Packham, C., et al., 2003, MNRAS, submitted

Pozzetti, L. & Mannucci, F. 2000, MNRAS, 317, L17

Ratnatunga, K. U., Griffiths, R. E., Casertano, S.,

Neuschaefer, L. W., & Wyckoff, E. W. 1994, AJ, 108, 2362

Ratnatunga, K. U., Griffiths, R. E., & Ostrander, E. J. 1999, AJ, 118, 86

Roche, N., Dunlop, J., & Almaini, O. 2003, ArXiv Astrophysics e-prints, 3206

Roche, N. D., Almaini, O., Dunlop, J., Ivison, R. J., & Willott, C. J. 2002, MNRAS, 337, 1282

Schlegel, D. J., Finkbeiner, D. P., & Davis, M. 1998, ApJ, 500, 525

Simard, L. 1998, in Astronomical Data Analysis Software and Systems VII, A.S.P. Conference Series, Vol. 145, 1998, R. Albrecht, R.N. Hook and H.A. Bushouse, eds., p.108, 108–+

Simard, L., Willmer, C. N. A., Vogt, N. P., Sarajedini, V. L., Phillips, A. C., Weiner, B. J., Koo, D. C., Im, M., Illingworth, G. D., & Faber, S. M. 2002, ApJS, 142, 1

Smail, I., Dressler, A., Couch, W. J., Ellis, R. S., Oemler, A. J., Butcher, H., & Sharples, R. M. 1997, ApJS, 110, 213

Smail, I., Ivison, R. J., Blain, A. W., & Kneib, J.-P. 2002a, MNRAS, 331, 495

Smail, I., Owen, F. N., Morrison, G. E., Keel, W. C., Ivison, R. J., & Ledlow, M. J. 2002b, ApJ, 581, 844, S02

Smith, G. P., Smail, I., Kneib, J.-P., Czoske, O., Ebeling, H., Edge, A. C., Pelló, R., Ivison, R. J., Packham, C., & Le Borgne, J.-F. 2002a, MNRAS, 330, 1

Smith, G. P., Smail, I., Kneib, J.-P., Davis, C. J., Takamiya, M., Ebeling, H., & Czoske, O. 2002b, MNRAS, 333, L16

Stanford, S. A., Eisenhardt, P. R., & Dickinson, M. 1998, ApJ, 492, 461

Steidel, C. C., Adelberger, K. L., Giavalisco, M., Dickinson, M., & Pettini, M. 1999, ApJ, 519, 1

Totani, T., Yoshii, Y., Iwamuro, F., Maihara, T., & Motohara, K. 2001, ApJ, 558, L87

Treu, T. & Stiavelli, M. 1999, ApJ, 524, L27

van Dokkum, P. G., Förster Schreiber, N. M., Franx, M., Daddi, E., Illingworth, G. D., Labbé, I., Moorwood, A., Rix, H., et al., 2003, ApJ, 587, L83

Vanzella, E., Cristiani, S., Arnouts, S., Dennefeld, M., Fontana, A., Grazian, A., Nonino, M., Petitjean, P., & Saracco, P. 2002, A&A, 396, 847

Wehner, E. H., Barger, A. J., & Kneib, J.-P. 2002, ApJ, 577, L83

Yan, L. & Thompson, D. 2003, ApJ, 586, 765, YT03

Zepf, S. E. 1997, Nature, 390, 377

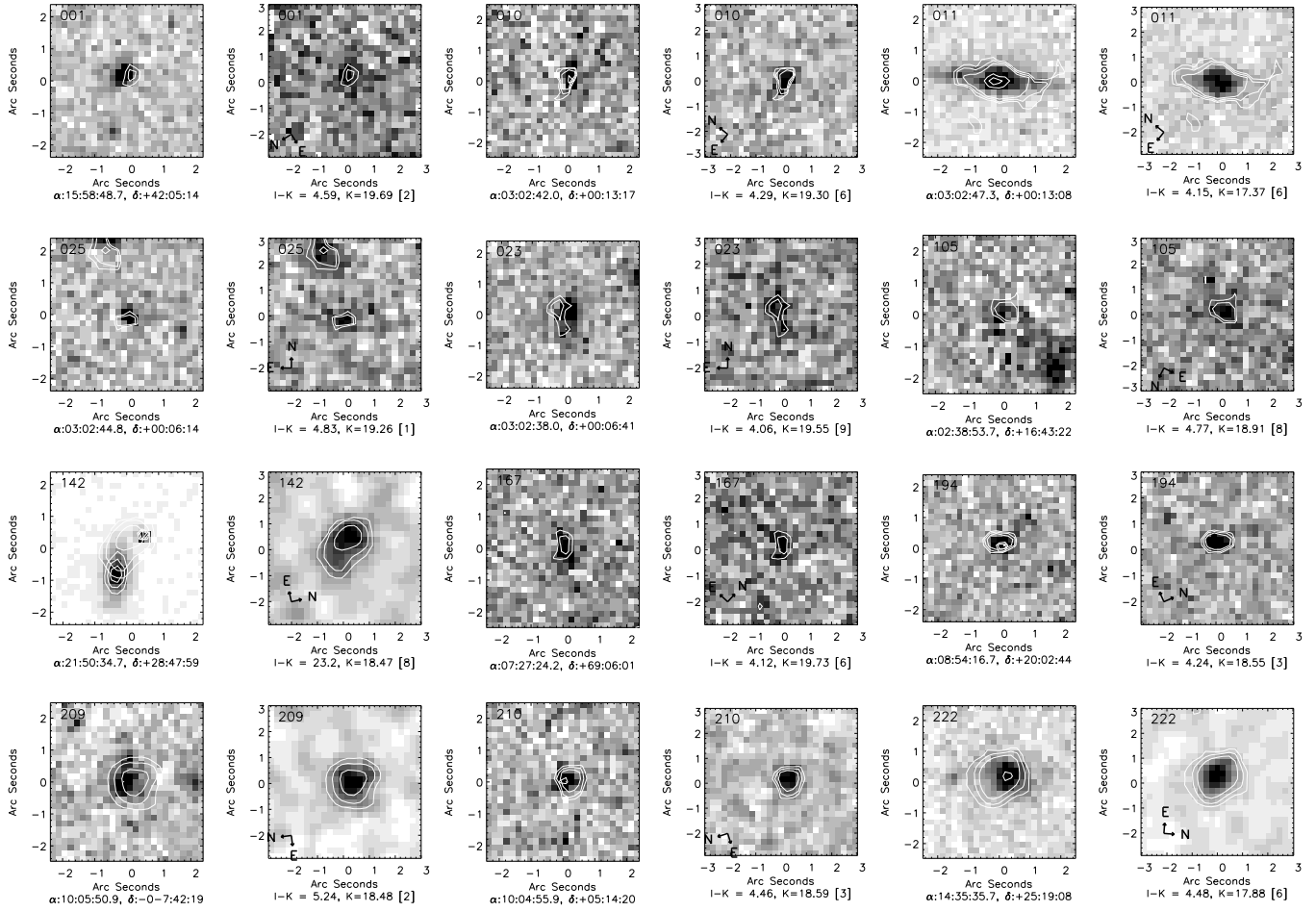


**Figure 11.** Thumbnail images of a examples of EROs. Each set of images comprises an F814W and  $K_s$ -band pair; ERO ID number is given in upper left. Left panel (labelled with R.A. and Dec.) is the non-resampled F814W image, rebinned  $2\times 2$  in its original orientation; right panel is  $K_s$ -band image, rotated to match the F814W orientation, with the vector indicating the orientation on sky. The label gives the  $(I - K)$  colour,  $K$  magnitude and visual morphological class in square brackets. The contours show the  $K_s$ -band isophotes. ERO11 is the largest disk in our sample. The  $K_s$ -band images appear overly smoothed as they have been resampled to match the (non-resampled) F814W image in this illustration, but are not resampled in our analysis.

**Table 6.** Example of our ERO catalogue. Columns show: ERO ID; Field name (derived from MDS naming); RA; Dec; Total  $K$ -band magnitude;  $I - K$  colour, MDS Maximum Likelihood classification; concentration index; visual morphological class; and comments. The full table is available in the electronic version of the journal.

ID#	Field	$\alpha$ (J2000)	$\delta$ (J2000)	$K_{\text{Tot}}$	$(I - K)$	MLE	C	Vis	Comments
001	U2AY2	15:58:48.7	+42:05:14	$19.69 \pm 0.14$	$4.60 \pm 0.13$	—	0.30	2	
002	U2AY2	15:58:50.5	+42:05:03	$19.63 \pm 0.17$	$4.33 \pm 0.13$	bulge	0.25	2	early-type?
003	U2AY2	15:58:46.5	+42:04:31	$18.79 \pm 0.09$	$4.20 \pm 0.07$	bulge	0.28	6	face-on spiral Sbc
004	U2H91	22:17:33.4	+00:15:04	$19.50 \pm 0.14$	$4.72 \pm 0.14$	—	0.33	3	
005	U2H92	13:12:11.4	+42:44:33	$19.69 \pm 0.04$	$4.31 \pm 0.05$	disk	0.36	3	
006	U2H92	13:12:14.1	+42:43:56	$19.67 \pm 0.04$	$4.42 \pm 0.04$	bulge	0.20	2	little Sa
007	U2H92	13:12:14.0	+42:43:06	$18.98 \pm 0.03$	$4.00 \pm 0.03$	d+bgal	0.24	6	face-on disk?
008	U2IY1	03:02:46.2	+00:13:45	$19.53 \pm 0.13$	$4.57 \pm 0.14$	disk	0.14	9	or merger (near chip edge)
009	U2IY1	03:02:46.5	+00:13:31	$19.54 \pm 0.15$	$4.95 \pm 0.15$	bulge	0.24	1	
010	U2IY1	03:02:42.0	+00:13:17	$19.30 \pm 0.13$	$4.29 \pm 0.10$	disk	0.19	6	edge-on late-type disk
...	...	...	...	...	...	...	...	...	...
...	...	...	...	...	...	...	...	...	...